SANDIA REPORT

SAND2016-8126
Unlimited Release
Printed June 2016

Progress in Overcoming Materials Challenges with Supercritical CO_2 Recompression Closed Brayton Cycles

Matthew S. Walker, Alan M. Kruizenga, Philippe F. Weck, Elizabeth A. Withey, Darryn D. Fleming, Gary E. Rochau

Prepared by
Sandia National Laboratories
Albuquerque, New Mexico 87185 and Livermore, California 94550

Sandia National Laboratories is a multi-program laboratory managed and operated by Sandia Corporation, a wholly owned subsidiary of Lockheed Martin Corporation, for the U.S. Department of Energy's National Nuclear Security Administration under contract DE-AC04-94AL85000.

Approved for public release; further dissemination unlimited.

Issued by Sandia National Laboratories, operated for the United States Department of Energy by Sandia Corporation.

NOTICE: This report was prepared as an account of work sponsored by an agency of the United States Government. Neither the United States Government, nor any agency thereof, nor any of their employees, nor any of their contractors, subcontractors, or their employees, make any warranty, express or implied, or assume any legal liability or responsibility for the accuracy, completeness, or usefulness of any information, apparatus, product, or process disclosed, or represent that its use would not infringe privately owned rights. Reference herein to any specific commercial product, process, or service by trade name, trademark, manufacturer, or otherwise, does not necessarily constitute or imply its endorsement, recommendation, or favoring by the United States Government, any agency thereof, or any of their contractors or subcontractors. The views and opinions expressed herein do not necessarily state or reflect those of the United States Government, any agency thereof, or any of their contractors.

Printed in the United States of America. This report has been reproduced directly from the best available copy.

Available to DOE and DOE contractors from
U.S. Department of Energy
Office of Scientific and Technical Information
P.O. Box 62
Oak Ridge, TN 37831

Telephone: (865) 576-8401
Facsimile: (865) 576-5728
E-Mail: reports@osti.gov
Online ordering: http://www.osti.gov/scitech

Available to the public from
U.S. Department of Commerce
National Technical Information Service
5301 Shawnee Rd
Alexandria, VA 22312

Telephone: (800) 553-6847
Facsimile: (703) 605-6900
E-Mail: orders@ntis.gov
Online order: http://www.ntis.gov/search

SAND2016-8126
Unlimited Release
Printed June 2016

Progress in Overcoming Materials Challenges with Supercritical CO_2 Recompression Closed Brayton Cycles

Matthew S. Walker[1], Alan M. Kruizenga[1], Philippe F. Weck[2], Elizabeth A. Withey[1], Darryn D. Fleming[3], Gary E. Rochau[3]

1. 8344: Materials Chemistry
2. 6225: Storage & Transportation Technologies
3. 6221: Advanced Nuclear Concepts
Sandia National Laboratories
P.O. Box 0969
Livermore, California 94551-MS9403

Abstract

The supercritical carbon dioxide (S-CO2) Brayton Cycle has gained significant attention in the last decade as an advanced power cycle capable of achieving high efficiency power conversion. Sandia National Laboratories, with support from the U.S. Department of Energy Office of Nuclear Energy (US DOE-NE), has been conducting research and development in order to deliver a technology that is ready for commercialization. There are a wide range of materials related challenges that must be overcome for the success of this technology. At Sandia, recent work has focused on the following main areas: (1) Investigating the potential for system cost reduction through the introduction of low cost alloys in low temperature loop sections, (2) Identifying material options for 10MW RCBC systems, (3) Understanding and resolving turbine degradation, (4) Identifying gas foil bearing behavior in CO_2, and (5) Identifying the influence of gas chemistry on alloy corrosion. Progress in each of these areas is provided in this report.

ACKNOWLEDGMENTS

Special acknowledgements to Farid El Gabaly Marquez for his contributions to this work through Raman and XPS Measurements, and to Joshua Sugar and Suzy Vitale for their valuable contributions through FIB and STEM Analyses. Robin Sharpe, Glenn Cannon, and Kirsten Norman have made significant contributions to the turbine degradation investigations.

Sandia National Laboratories is a multi-program laboratory managed and operated by Sandia Corporation, a wholly owned subsidiary of Lockheed Martin Corporation, for the U.S. Department of Energy's National Nuclear Security Administration under contract DE-AC04-94AL85000.

CONTENTS

FIGURES

TABLES

NOMENCLATURE

$S\text{-}CO_2$	Supercritical Carbon Dioxide
US DOE-NE	United States Department of Energy – Nuclear Energy Division
RCBC	Recompression Closed Brayton Cycle
CBC	Closed Brayton Cycle
ASME	American Society of Mechanical Engineers
MAGNOX	Magnesium Non-Oxidizing (Type of nuclear reactor designed in the UK)
AGR	Advanced Gas-cooled Reactor
HCl	Hydrochloric Acid
SEM	Scanning Electron Microscope
FIB	Focused Ion Beam
TEM	Transmission Electron Microscopy
STEM	Scanning Transition Electron Microscopy
HAADF	High-Angle-Annular-Dark-Field
XPS	X-ray Photoelectron Spectroscopy
XRD	X-ray Diffraction
TIT	Turbine Inlet Temperature
EDS	Energy Dispersive Spectroscopy
RCA	Root Cause Analysis
TAC	Turbine - Alternator – Compressor
FMA	Failure Mode Assessment
TPR	Technical Plan of Resolution
NDA	Non-Disclosure Agreement
EBSD	Electron Backscatter Diffraction

1. INTRODUCTION

The supercritical carbon dioxide (S-CO2) Brayton Cycle has gained significant attention in the last decade as an advanced power cycle capable of achieving high efficiency power conversion; it represents a thermal to electric energy conversion system with an efficiency approaching 50% under the operating conditions required for advanced energy systems. Sandia National Laboratories, with support from the U.S. Department of Energy Office of Nuclear Energy (US DOE-NE), has been conducting research and development in order to deliver a Recompression Closed Brayton Cycle (RCBC) that is ready for commercialization. There are a wide range of materials related challenges that must be overcome for the success of this technology. At Sandia, recent work has focused on the following main areas: (1) Investigating the potential for system cost reduction through the introduction of low cost alloys in low temperature loop sections, (2) Identifying material options for 10MW RCBC systems, (3) Understanding and resolving turbine degradation, (4) Identifying gas foil bearing behavior in CO_2, and (5) Identifying the influence of gas chemistry on alloy corrosion. Progress in each of these areas is provided in this report.

PAGE INTENTIONALLY LEFT BLANK

2. EVALUATING THE INTRODUCTION OF LOW COST ALLOYS IN LOW TEMPERATURE LOOP SECTIONS

2.1. Background

Developing a system with satisfactory capital costs is critical to the success of this mission. Heat exchangers play a critical role in S-CO_2 Closed Brayton Cycles (CBC), as significant recuperation in addition to the heat input and removal are required in order to achieve the high efficiencies associated with the proposed cycles [1], yet these are also expected to be the largest components in any S-CO_2 CBC, resulting in a significant portion of the overall cycle costs [2]. It is estimated that heat exchangers alone account for 40% of the Sandia RCBC test loop total capital costs. There is interest in identifying opportunities for balance of plant cost optimization. One possibility for this is a shift to more inexpensive alloys for the lower temperature portions of the system. While the system temperatures range from room temperature up to 565^{o}C, a significant portion of the system piping remains at less than 260^{o}C. This is evident in Figure 1, where a diagram of the test loop indicates portions of the loop piping at less than 260^{o}C. While more expensive alloys (stainless steels and super alloys) are necessary for the higher temperature portions of the system, it may be possible to introduce inexpensive carbon steel into the lower temperature portions of the loop as a replacement for 316 stainless steel. Supporting this idea, at 30 MPa and 330^{o}C, the ASME Power Piping Code B31.1 indicates the same required pipe wall thickness (0.25") for carbon steel as for 316 steel.

Corrosion experiments in S-CO_2 have focused predominantly on the expensive alloys for the aggressive (in terms of temperature and pressure) portions of these systems. Experimental data for inexpensive carbon steel alloys in this environment are sparse, while the impact of CO_2 corrosion on carbon steel has been studied extensively at pressures relevant for oil and gas transport (up to 2 MPa)[3]. The best information that exists relating to the performance of carbon steel in more relevant CO_2 environments comes from work done as part of the British MAGNOX and AGR nuclear reactor programs[4-9]. Much of this work was focused on understanding mechanisms for the breakaway oxidation that was observed under conditions relevant to these reactors. It appears that carbon steel is often susceptible to this enhanced form of attack in high pressure CO_2 environments at 350 – 500^{o}C. With regards to the corrosion rate in a relevant S-CO_2 environment, there was some work done at Idaho National Laboratory where they report a corrosion rate of 0.01 mm/year for iron over a period of approximately 5000 hrs at 162-183^{o}C and 8.7 – 12.3 MPa [10].

In this study, the corrosion performance of a mild carbon steel alloy (X65Q) was evaluated in S-CO_2 at 263^{o}C and 17.6 MPa, for exposure durations up to 2000 hours. The X65Q alloy was selected for this work as it is an alloy which satisfies three of the specifications (A53, A106, and API-5L) within the ASME Power Piping Code B31.1.

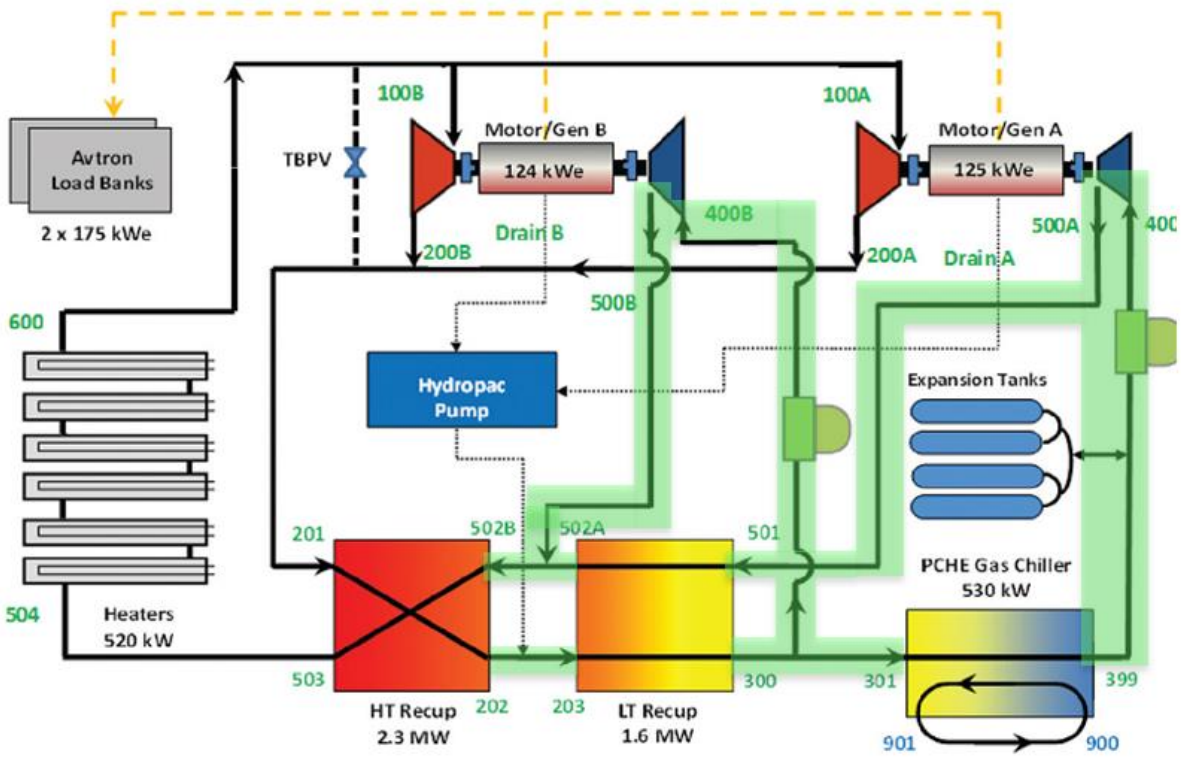

Figure 1. System diagram for Sandia's RCBC test loop (shaded green areas indicate T<260°C).

2.2. Approach

2.2.1. Corrosion tests

The nominal composition of X65Q steel is listed in Table 1. The test samples were 32 mm diameter disks with a thickness of 1.5 mm. The samples were ground to 120 grit surface finish to replicate the surface finish of actual components. The specimens were ultrasonically cleaned in ethanol and acetone prior to exposure and suspended from an alumina rod with alumina spacers between individual specimens. A photograph of the sample holder is shown in Figure 2. The samples were tested for an exposure duration of 2000 hours, with samples being removed at intervals of 500 hours for analysis. Six samples were removed for analysis at each time interval.

Table 1. Element compositions (wt.%) in X65Q

Fe	C	Mn	P	S	Si	Cu	Ni	Cr	Mo	Al	V	B	Ti	Nb
Bal	0.15	0.97	0.012	0.003	0.18	0.09	0.05	0.07	0.11	0.31	0.034	0.0003	0.003	0.002

Figure 2. Photograph of the Inconel 625/Alumina sample holder.

The S-CO_2 corrosion test facility that was developed at Sandia National Laboratories for these experiments utilizes an autoclave fabricated from Inconel 625 within a two-zone heated furnace. The autoclave has interior dimensions of 51 mm diameter by 610 mm length, and is rated to 650^{o}C at 31 MPa. A photograph of the corrosion test setup is shown in Figure 3.

Industrial grade CO_2 with a purity of 99.5% was fed in a liquid state from a commercial cylinder (~ 5.7 MPa / 830 psi) to a Supercritical 24 constant flow dual piston pump, which subsequently supplied S-CO_2 to the autoclave chamber. A pressure transducer installed between this pump and the autoclave chamber is used to monitor pressure; S-CO_2 flow out from the pump is adjusted to provide the target chamber pressure as measured by this transducer. Autoclave temperature is measured using three thermocouples across the chamber length. Throughout this experiment the system was controlled to provide a pressure of 17.6 ± 0.2 MPa and a temperature of 263 ± 3^{o}C.

Figure 3. Photograph of the Sandia S-CO_2 corrosion test facility.

Two methods were used for evaluating the extent of sample corrosion. One method was to measure the sample weight gain as a function of test exposure time. For this, mass change due to corrosion was measured on an A&D model GH-252 balance (± 0.03 mg accuracy). While this method provides an indication of oxidation rate (rate of sample oxygen pickup through oxidation), it is difficult to extract a corrosion rate from this that could be used for making material lifetime predictions.

The second method enables lifetime predictions through the chemical removal of corrosion products from the samples, providing data for unaffected remaining metal as a function of exposure time. Three chemical descale treatments were selected from the ASTM Standard Practice for Preparing, Cleaning, and Evaluating Corrosion Test Specimens [11] and evaluated as part of this work. The three solutions used are listed in Table 2. Using samples from the first time interval, 500 hours exposure, each of the three solutions was evaluated; six descale cycles of 10 minutes each were used for this. The descale weight loss data for the three solutions is shown in Figure 4. While each of the solutions was effective at removing the sample corrosion products, two of the solutions (Diammonium Citrate and HCl) exhibited extensive attack of the base metal. Based on this evaluation, the HCl-Hexamine solution was selected as the optimum solution to use for this study.

Table 2. Solutions evaluated for chemical descale of sample corrosion products

Solution	Solution Temp (^{o}C)	Cycles	Cycle Duration (min)
6M HCl (21 wt %)	20-25	6	10
6M HCl (21 wt %) + Hexamethylene tetramine (0.3 wt %)	20-25	6	10
Diammonium Citrate (20 wt %)	75-90	6	10

Using the HCl-Hexamine solution, descale weight loss data for samples at each of the time intervals are shown in Figure 5. It appears from this data that one 10 minute cleaning cycle is adequate for removing the corrosion products for samples with up to 2000 hours exposure; additional cleaning cycles appear to remove the base metal. For each exposure time, the descale weight loss after the first cleaning cycle is representative of its extent of corrosion. In this way, corrosion rate can be calculated for each time interval, incorporating this mass loss into Equation (1) below. The surface area for each sample was precisely measured prior to the experiment. An alloy density of 7.85 g/cm^3 is used for these calculations; this is the density for mild steel.

$$Corrosion\ Rate\ (mm/y) = \frac{8.76x10^4 * Mass\ Loss\ (g)}{Area\ (cm^2) * Alloy\ Density\ (g/cm^3) * Time\ (hrs)} \qquad (1)$$

For the six samples extracted at each time interval, weight gain was measured for all six samples. Three of the six samples were subjected to the HCl-Hexamine descale treatment for weight loss measurements. The other three samples were utilized for microstructural and surface chemistry characterization.

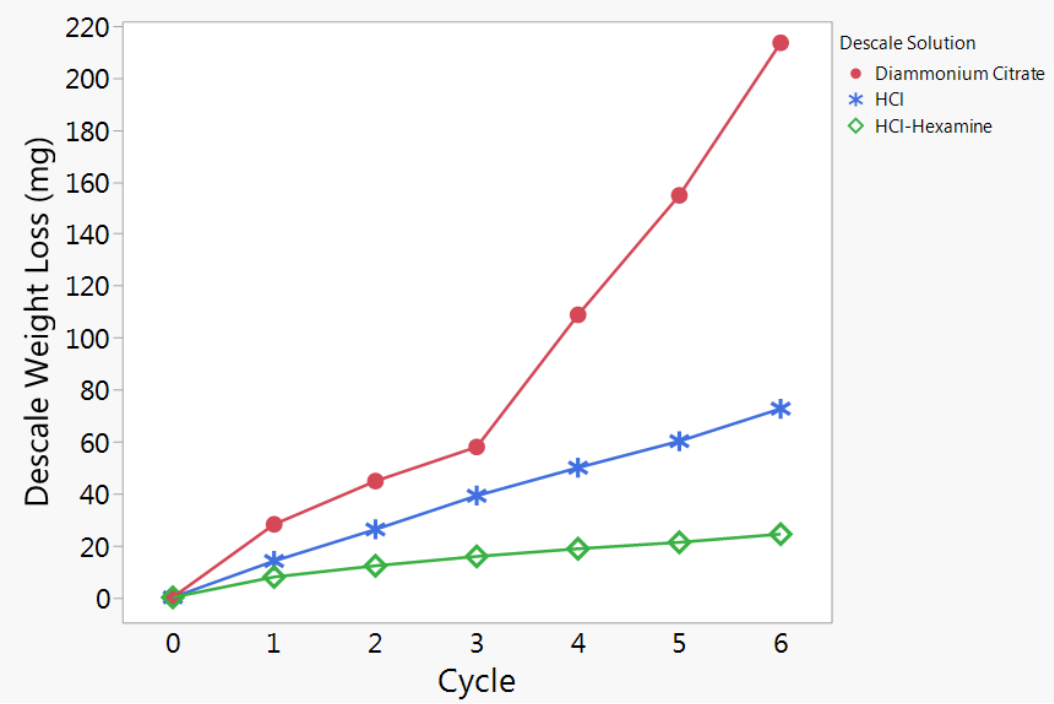

Figure 4. Descale weight loss compared for three chemical solutions over 6 descale cycles.

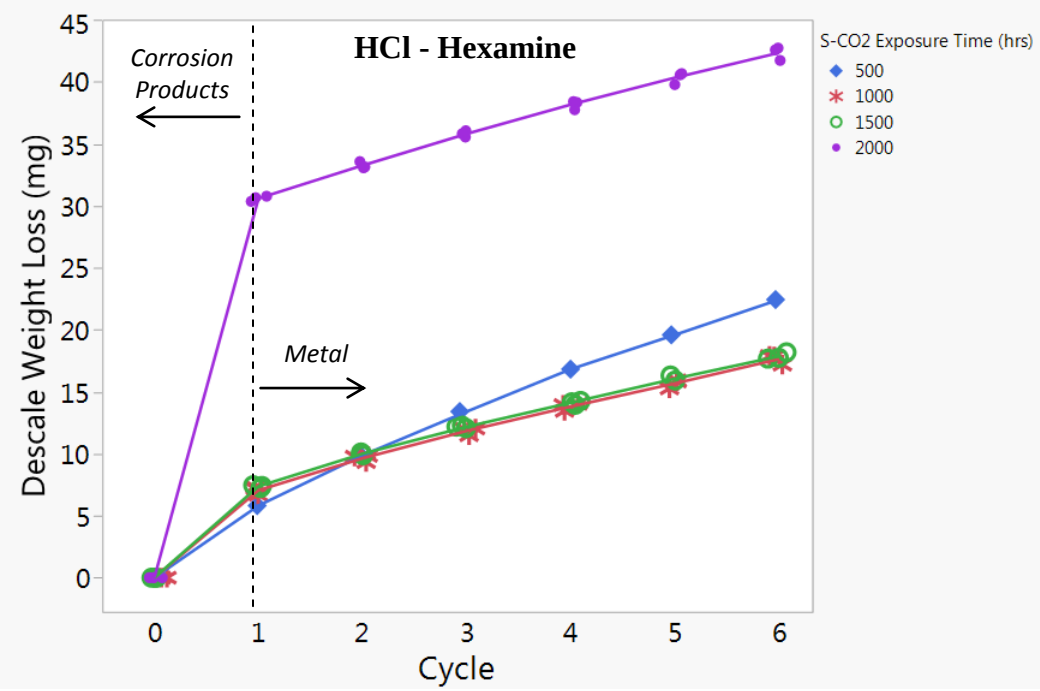

Figure 5. Sample descale weight loss compared across the different S-CO2 exposure times.

2.2.2. Microstructural characterization

Low magnification surface oxide morphology analysis was performed with a Keyence VHX-2000 optical microscope. Detailed images of the surface oxide were obtained using an FEI Phenom tabletop scanning electron microscope (SEM). Cross-sectional samples were prepared in an FEI Helios 660 Nanolab focused ion beam (FIB). Prior to extracting cross-sectional lamellae a carbon coating was deposited to protect the oxide surface. Thin lamellae were milled from 500- and 2000-hr samples using a standard in-situ lift-out method for transmission electron microscopy (TEM) samples. Imaging of the oxide layers was accomplished via the scanning transmission electron microscopy (STEM) mode in the FIB using bright field and high-angle-annular-dark-field (HAADF) detectors. Oxide thicknesses were measured directly from the HAADF images.

2.2.3. Surface characterization

Several different complimentary techniques were used to identify the chemistry of the corrosion products formed on the samples in S-CO_2. These are important as several different phases of iron oxide may form on carbon steel. The three techniques used for corrosion product chemistry include X-ray photoelectron spectroscopy (XPS), Raman spectroscopy, and X-ray diffraction (XRD).

For XPS characterization, spectra were obtained with an Al Kα source (Omicron model DAR400) using photons of 1490 eV. Photoelectrons were detected using a Physical Electronics model 10-360 electron energy analyzer. XPS was calibrated by adjusting the binding energy of the most prominent C 1s peak to 284.8 eV. The spectra were processed by the CasaXPS software using a Shirley-type background subtraction.

Raman spectroscopy was performed using a Renishaw InVia Micro-Raman spectrometer in air using a backscattering geometry with a 50X objective lens, a frequency-doubled Nd:YAG laser, and a CCD detector. The images scan used a step size of 0.5 μm.

XRD was performed using a PANalytical Empyrean unit. Using Copper K□ as the x-ray source, scans were conducted from 10 to 100 degrees 2□ (^{o}2□) with a step size of 0.013 ^{o}2□. A scan step time of 129 seconds was use for these analyses. HighScore software was used for identifying chemical phases of the obtained diffraction patterns [12].

2.3. Results

2.3.1. Corrosion measurements

The weight gain data for samples after exposure to S-CO_2 for every 500 hours up to 2000 hours is shown in Figure 6. Six samples were measured at each 500 hour time interval. The values plotted are the average weight gain values. Error bars are included to indicate the range of weight gain among each set of samples. The rate of weight gain (i.e. oxidation) levels off starting around 1000 hours indicating that the oxide scale, which forms on the alloy, becomes protective after this initial exposure period. Starting around 1500 hours exposure, the oxide scale appears to lose its protective capability, as the rate of weight gain rapidly increases. The rapid increase in corrosion rate is indicative of breakaway corrosion; for this particular alloy the time to breakaway corrosion is 1500 hours.

For samples with S-CO_2 exposure up to 2000 hours, the sample weight loss after one chemical descale cycle is shown in Figure 7. Again, average weight loss values are plotted. Three samples were measured at each 500 hour time interval, and error bars are included to indicate the range of weight loss among each set of samples. These sample weight loss values are consistent with the sample weight gain measurements, as the same trends in the data were observed.

The sample weight loss data can be used to calculate the corrosion rate for this particular alloy under the conditions of this test. Due to breakaway oxidation being observed for these samples, it is most useful to calculate the post-breakaway corrosion rate. In this way, the corrosion rate is calculated using Equation (1) along with the post-breakaway rate of sample weight loss from Figure 7 (slope of line between 1500 and 2000 hours S-CO_2 exposure). This gives an average sample corrosion rate of 0.032 mm/year (1.25 mils/year).

2.3.2. Microstructural characterization

Optical micrographs of representative samples from 500, 1000, 1500, and 2000 hour treatment increments are shown in the left column of Figure 8. The samples darken in color with increasing exposure time up to 1000 hours with little change at longer exposure duration. It is assumed that the lighter non-uniform color of the 500 hour samples is indicative of incomplete coverage of the surface by oxide. With increasing time, the SEM micrographs in the right two columns of Figure 8 indicate an increasing amount of surface oxide growth. Also, while islands of surface oxide appear on the sample surfaces, oxide is also present to varying degrees along the entire surface. At 2000 hours, this surface oxide shows distinct cracks which correlate with the breakaway portions of the weight gain/loss curves.

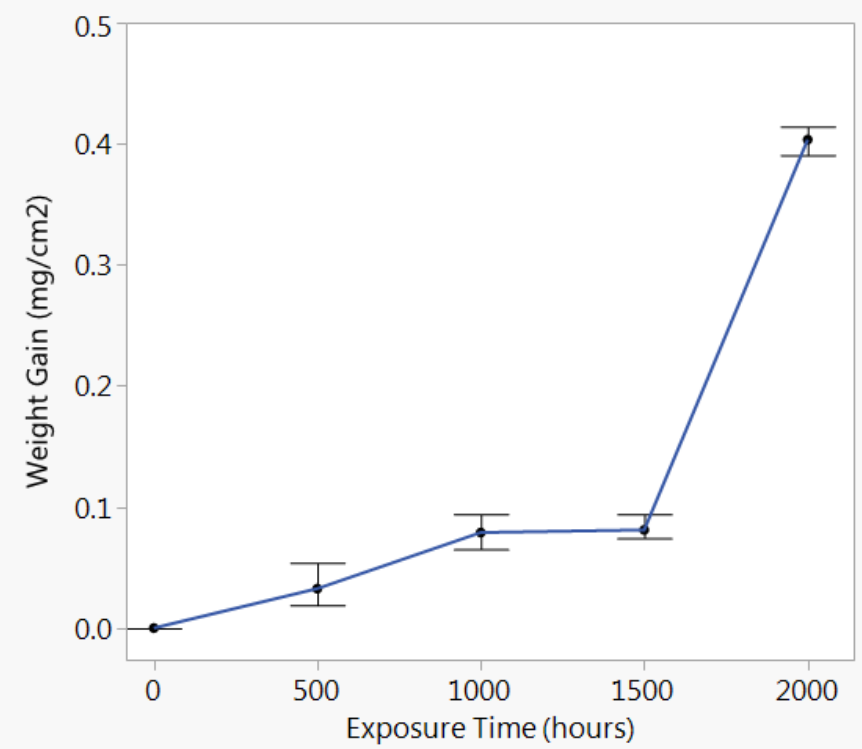

Figure 6. Weight gain due to corrosion after exposure to S-CO_2 from 500 to 2000 hours.

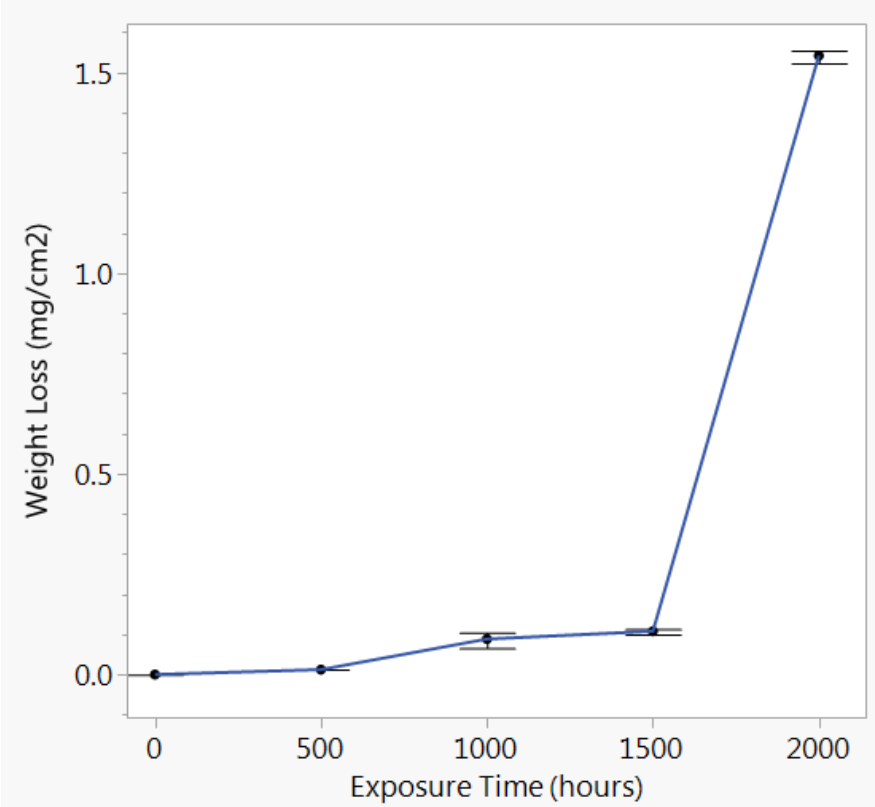

Figure 7. Weight loss of corroded samples resulting from one chemical descale cycle.

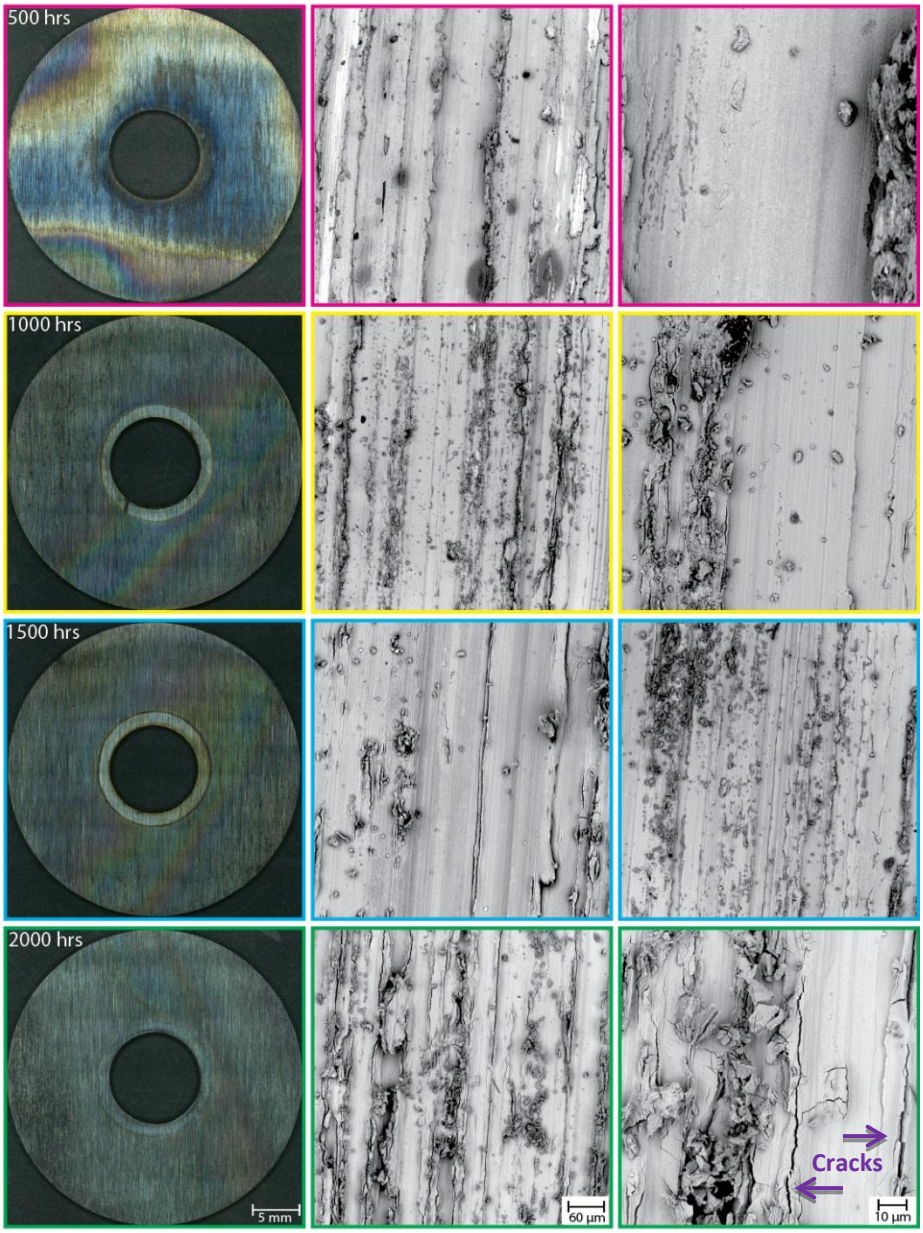

Figure 8. Optical micrographs (left column) and SEM images taken at 500X (middle column) and 2400X (right column) magnifications.

Images from the FIB cross-section samples are shown in Figure 9. The locations of the thinned lamellae, shown in the right two columns, are indicated by the arrows and labels in the left most column. Samples were extracted from areas of different surface topography; this includes raised areas or peaks as well as lower areas or valleys. This topography, with periodic waviness, is believed to result from the starting surface roughness of the samples. In both samples, the oxide layer is thicker on the peaks (B and D) than the valley areas (A and C). Multiple oxide layers are evident in regions where the oxide is thick; it is possible to designate these as three distinct layers. On the peak areas of both samples, and the valley area of the 2000-hr sample, the top

oxide layer is ~ 25-70 nm thick followed by an intermediate layer that is up to 500 nm thick. The thickness of the oxide layer closest to the base metal (bottom layer) varies greatly between the two samples and is location dependent. At 500 hours, the intermediate and bottom oxide layers are not observed in the valley region. However, three distinct oxide layers are observed along the peak areas of the 500 hr sample and in both areas of the 2000 hr sample. The bottom layer increases in thickness from 500 nm along the peak area of the 500 hr sample to over 3 µm in the 2000 hr sample. This layer also appears to be denser in the 2000-hr sample. It should be noted that the color of the bottom oxide layer is darker than those nearer to the surface.

In Figure 10 the measured oxide layer thicknesses are compared between samples at the two S-CO_2 exposure times. Here, the thicknesses are shown for the three distinct layers observed, and this is shown for both the peak and valley areas along the sample surfaces. This plot reveals that the large increase in overall oxide thickness going from 500 hrs to 2000 hrs is dominated by growth of the bottom-most oxide layer that sits next to the base metal. It is reasonable to associate the growth of this bottom oxide layer to the breakaway portion of the weight gain/loss curves.

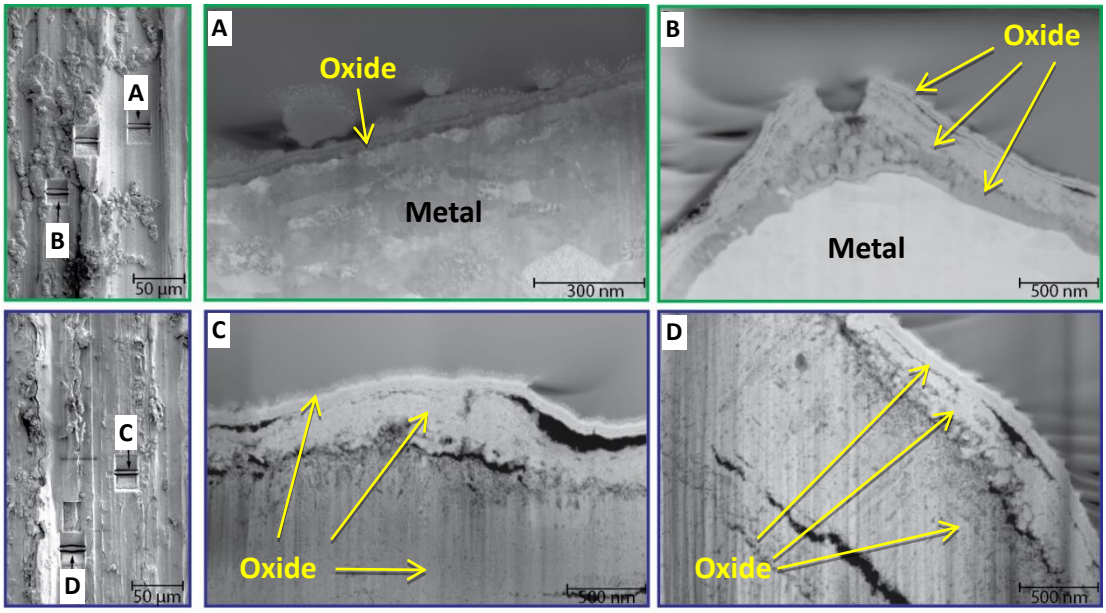

Figure 9. SEM overview of sample surface in FIB indicating the location of lift out samples (left column and STEM HAADF images of thinned lamellae in flat (middle column) and raised (right column) areas. The 500 hour sample is shown in the top row and the 2000 hr sample in the bottom row.

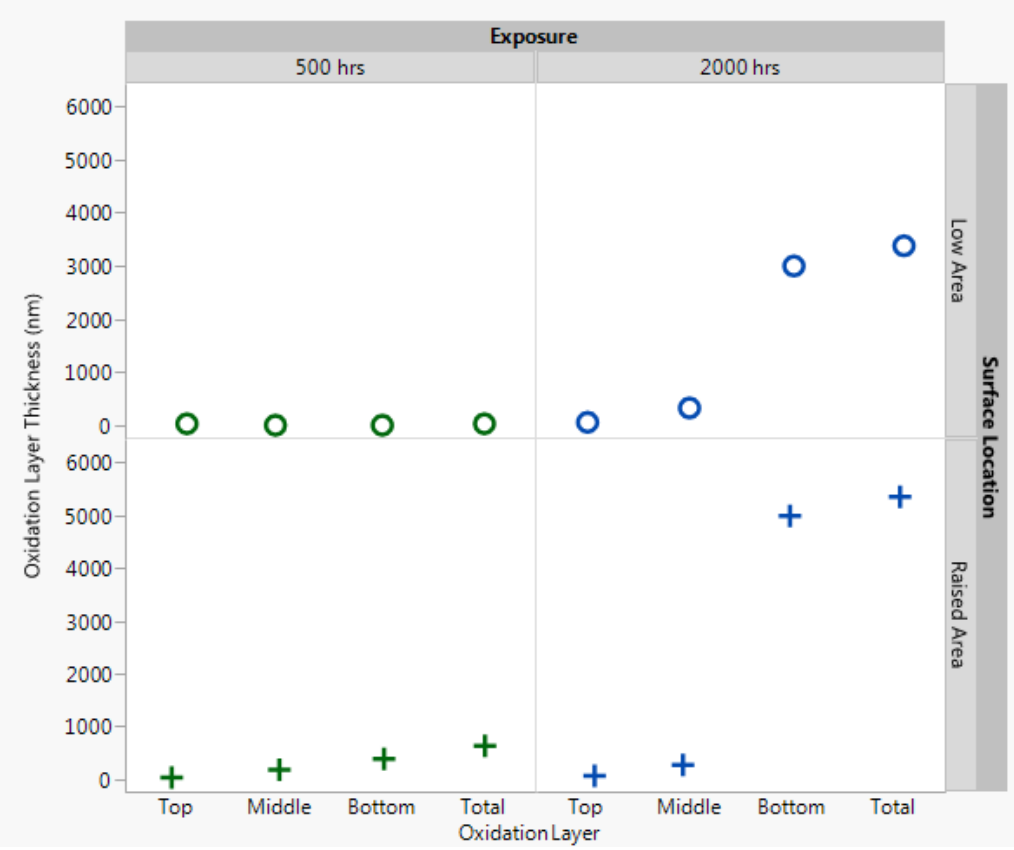

Figure 10. Oxidation layer thickness changes from 500 to 2000 hours S-CO_2 exposure.

2.3.3. Surface characterization

Information about corrosion product chemistry at sample surfaces was obtained by XPS. This has a very shallow probing depth (2-3 nm), and so this can provide the chemistry of the top-most layer on the samples. Figure 11 shows the XPS spectra of the Fe 2p core level for both a 500 hr and 2000 hr sample. Here the Fe^{2+} and Fe^{3+} contributions are colored red and blue, respectively. The results indicate a contribution only from Fe^{3+} for both samples, with the contribution being stronger for the 2000 hr sample versus that for the 500 hr sample. From this analysis, it appears that the oxide layer on the outer surface of these samples is hematite (Fe_2O_3).

Raman spectroscopy, having a significantly deeper probing depth (> 1μm) than XPS, is able to provide chemistry information across the multiple oxide layers for these samples. Analysis for multiple areas of 500 hr and 2000 hr sample surfaces indicated the presence of both hematite (Fe_2O_3) as well as magnetite (Fe_3O_4) in each instance. X-ray diffraction of a 2000 hr sample surface further supports these results, as both hematite and magnetite peaks were present in the diffraction pattern. The XRD pattern for the 2000 hr sample is shown in Figure 12. Collectively these analyses provide evidence that the oxidation layer consists of an outer hematite layer along with an inner magnetite layer.

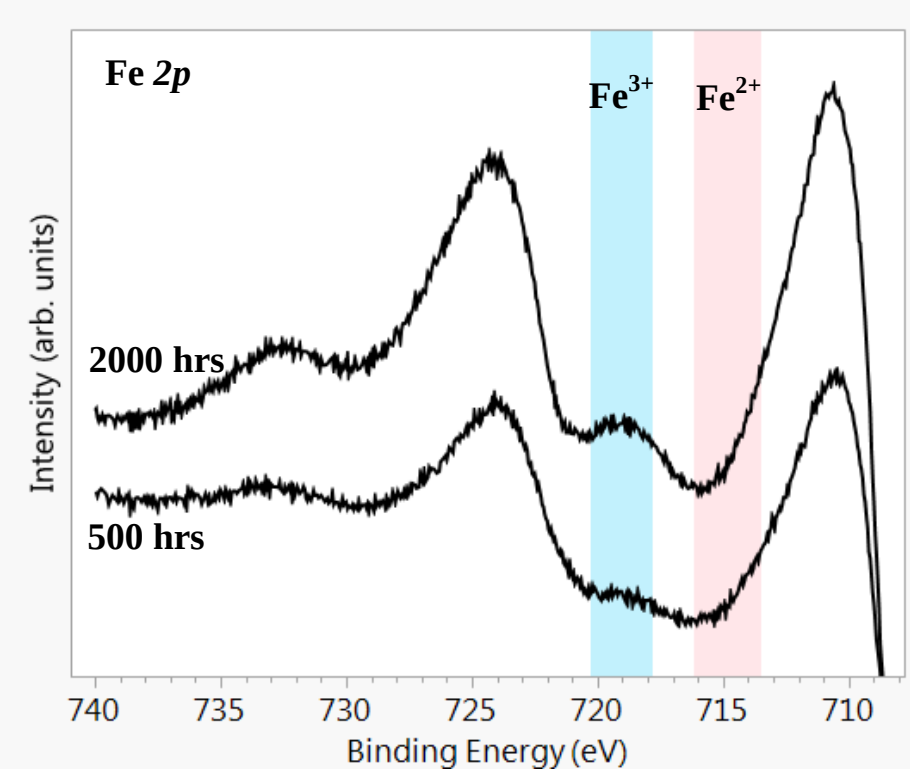

Figure 11. Fe 2p photoelectron spectra from sample surfaces at 500 and 2000 hrs exposure.

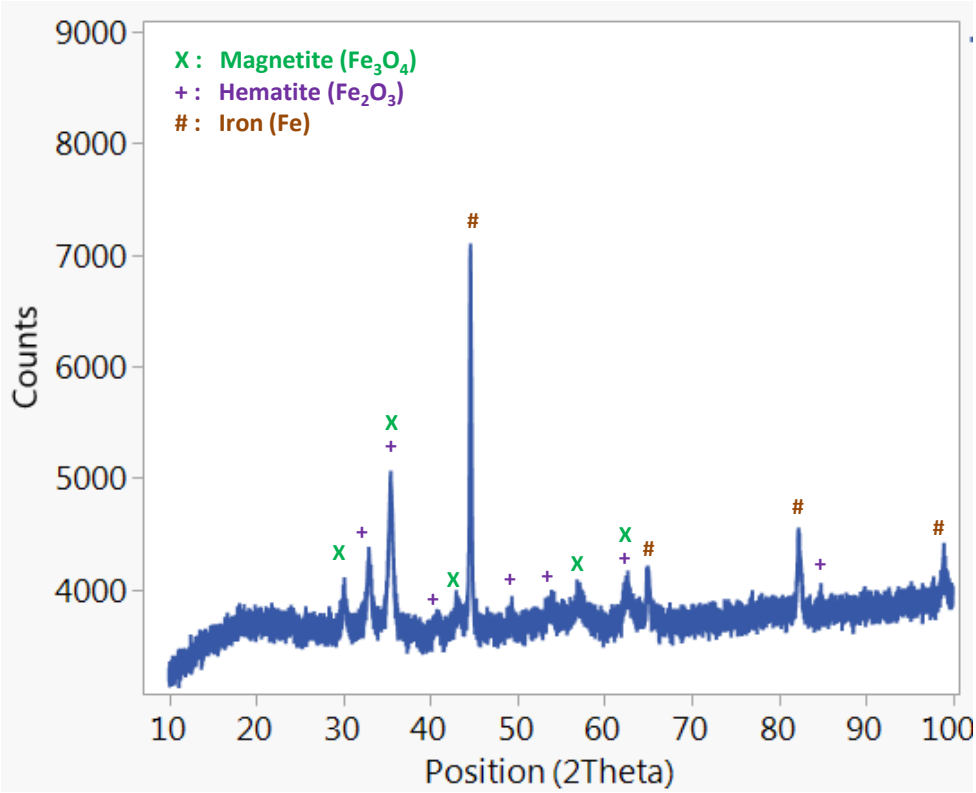

Figure 12. Surface X-ray diffraction pattern for sample with 2000hrs S-CO_2 exposure.

2.4. Summary and Next Steps

Corrosion behavior of a carbon steel alloy (X65Q) was measured at 260°C and 17.6 MPa for up to 2000 hours S-CO_2 exposure. This inexpensive alloy is being explored as a replacement for more expensive stainless steel alloys in low to intermediate temperature portions of Sandia's closed Brayton loop. Corrosion was measured by two methods, both exhibiting the same behavior. The alloy forms an initial protective oxide scale, which after 1500 hours loses its ability to protect the base metal, resulting in breakaway oxidation with a measured corrosion rate of 0.032 mm/year. Transition to breakaway oxidation is attributed to cracks which form in the surface oxide, resulting in preferential growth of a thick magnetite (Fe_3O_4) layer beneath a hematite (Fe_2O_3) outer layer. Cracks in the hematite outer layer, enable CO_2 transport closer to the base metal surface, reducing the barrier (bulk Fe diffusion through the oxide scale) to the iron oxidation reaction. Despite the transition of the oxide scale from protective to breakaway after 1500 hours, the post-breakaway corrosion rate is still rather small. Predicted lifetimes based on this corrosion rate are very long, in excess of 50 years.

Prior to making the switch to inexpensive alloys for low temperature system piping, a few areas exist where additional data is needed. Most prominent is an assessment of carbon steel compatibility in connection to other alloy components; the concern here is dissimilar metal induced corrosion. A second area is susceptibility to oxide spallation resulting from longer term exposure and/or more representative pipe geometry, versus the flat washer samples used for this investigation.

PAGE INTENTIONALLY LEFT BLANK

3. IDENTIFYING MATERIAL OPTIONS FOR 10MW RCBC SYSTEMS

3.1. Background

Developing a system with satisfactory capital costs is critical to the success of this mission. Heat exchangers play a critical role in S-CO_2 Closed Brayton Cycles (CBC), as significant recuperation in addition to the heat input and removal are required in order to achieve the high efficiencies associated with the proposed cycles [1], yet these are also expected to be the largest components in any S-CO_2 CBC, resulting in a significant portion of the overall cycle costs [2]. It is estimated that heat exchangers alone account for 40% of the Sandia RCBC test loop total capital costs. There is interest in identifying opportunities for balance of plant cost optimization. One possibility for this is a shift to more inexpensive alloys for the lower temperature portions of the system. While the system temperatures range from room temperature up to 565^{o}C, a significant portion of the system piping remains at less than 260^{o}C. This is evident in Figure 1, where a diagram of the test loop indicates portions of the loop piping at less than 260^{o}C. While more expensive alloys (stainless steels and super alloys) are necessary for the higher temperature portions of the system, it may be possible to introduce inexpensive carbon steel into the lower temperature portions of the loop as a replacement for 316 stainless steel. Supporting this idea, at 30 MPa and 330^{o}C, the ASME Power Piping Code B31.1 indicates the same required pipe wall thickness (0.25") for carbon steel as for 316 steel.

3.2. Approach

The goal for this work is the establishment of a database that can be used to facilitate alloy selection for 10MW RCBC systems at the two turbine inlet temperatures (TIT) of 550^{o}C and 700^{o}C. The path that has been laid out for achieving this goal is shown in Figure 13. The first step in this process is to establish 10MW system designs at both TIT's. From these system designs, the exposure conditions (T, P) and performance requirements (i.e. weldability, creep strength, etc.) for each component are established.

Knowing the exposure conditions for each component provides the framework for mining the literature for relevant alloy performance data. Literature to be mined includes the ASME Pipe Code along with alloy corrosion rate data from other sources. The ASME Pipe Code provides the required material thickness for a range of alloys over the relevant conditions, but this does not take corrosion into account. Other literature (journal articles, theses, technical reports, etc.) are mined for alloy corrosion rates over the same conditions. Together, these provide the information needed to estimate the material thicknesses required to meet the desired lifetime under these conditions.

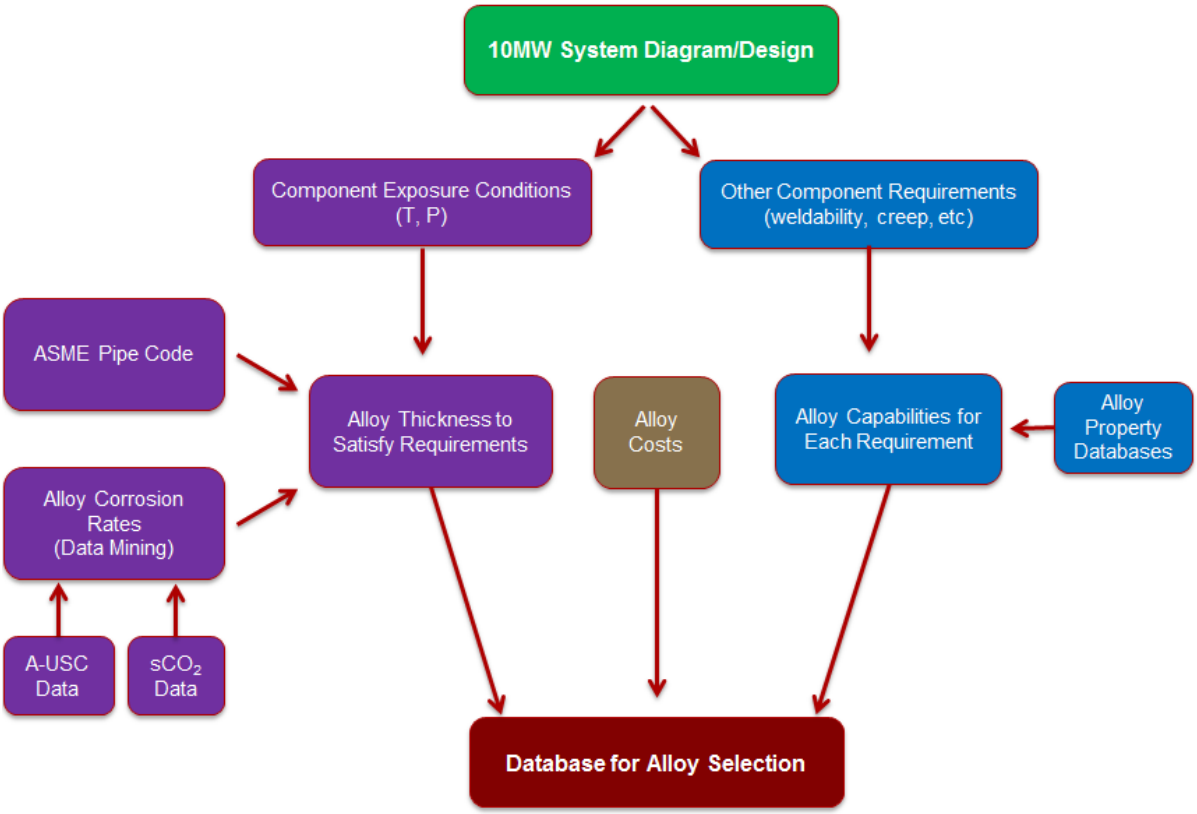

Figure 13. Process flow diagram for the creation of an S-CO2 system alloy selection database.

Each component of the 10MW RCBC system serves a particular function. As such, there are performance requirements associated to each; these may include weldability, creep strength, among others. In developing a database to facilitate component alloy selection, it is important to evaluate the range of alloys against these performance requirements. This is done by first defining the performance requirements for each component, and second by mining alloy property data over each performance requirement.

It is likely that alloy corrosion rate data and/or property data is not available over all of the exposure conditions. While this may impart gaps in the database for some components, it is imperative to identify these gaps as areas of needed future research. In this way, the database developed as part of this work is viewed as a starting point, to be expanded in the future as more data becomes available.

The final component to building this database is the economic consideration for each alloy. Alloy costs need to be considered alongside the range of possible alloys for each component. For some components there may be multiple alloys that can satisfy the requirements. Comparing the costs for each alloy together with its required thickness is instrumental in making decisions on the optimal alloy.

3.3. Results

10 MW RCBC system designs for wet cooling conditions at both 550^{o}C and 700^{o}C TIT's have been established by our colleague at Sandia –Albuquerque (Jim Pasch); these are shown in Figure 14 and Figure 15 respectively for each temperature. Using these flow sheets, the system is broken out into 8 separate components: Turbine, Re-Compressor, Main Compressor, Heater, High Temperature (HT) Recuperator, Low Temperature (LT) Recuperator, Gas Cooler, and Piping. Piping is unique versus the other components, in that it covers a range of exposure conditions. So, piping is broken down further into separate components for its 8 sets of exposure conditions; these are shown as A through H on Figure 14 and Figure 15. This give a total of 15 system components, including 7 which are non-piping and 8 which are piping.

Component exposure conditions have been extracted from both flow sheets, providing the information needed to mine the literature for relevant alloy performance data. These exposure conditions are summarized graphically in Figure 16, where component temperatures are shown as red (550^{o}C TIT) and blue (700^{o}C TIT) bars and pressure as green dots. This same information for component temperature can be utilized to create the flow sheet temperature maps shown Figure 17. Both of these are useful for understanding how component temperature requirements change as a function of TIT. Along these lines, it is evident in Figure 16, that moving to the higher TIT (700^{o}C) only impacts the exposure temperature for 6 of the 15 components, while the others remain unchanged. Also, it is evident in both Figure 16 and Figure 17, that a significant portion the system (9 out of the 15 components) remains at low exposure temperature (<260^{o}C) regardless the TIT.

A literature search was recently completed which has provided over 50 sources for alloy corrosion data in S-CO2. Alloy corrosion data is being mined from these sources and compiled into an excel spreadsheet database. It is expected that there will be component exposure conditions for which data does not exist. These will be highlighted as areas of need for future research. Also, for the time being, corrosion data from other environments (i.e. A-USC) will be sought at these exposure conditions in order to allow for preliminary alloy selection.

In addition to identifying corrosion data that is relevant to each component, work to identify other performance requirements of each component has started using assistance from Antonio Garcia at Quantigy LLC. These are being compiled into an excel spreadsheet database together with alloy property data for each requirement. The integration of this database together with alloy cost and alloy thickness requirement databases, will ultimately enable the construction of a single alloy selection database for all components.

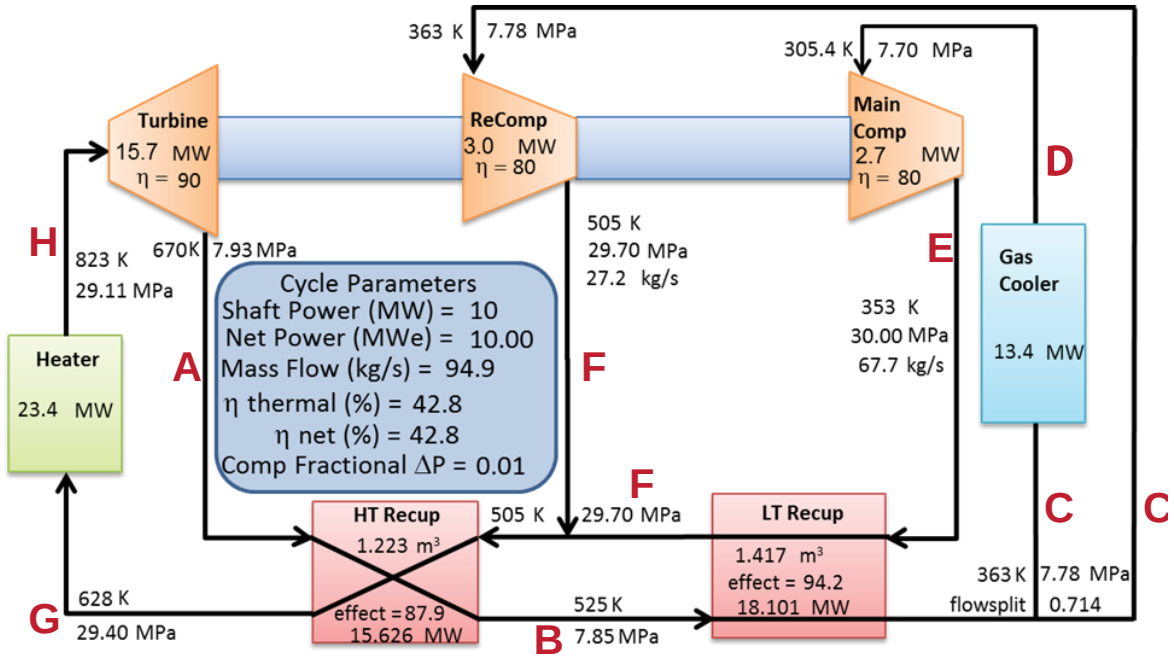

Figure 14. RCBC Flow Sheet for Wet Cooling Conditions, 550°C TIT, at 10 MWe.

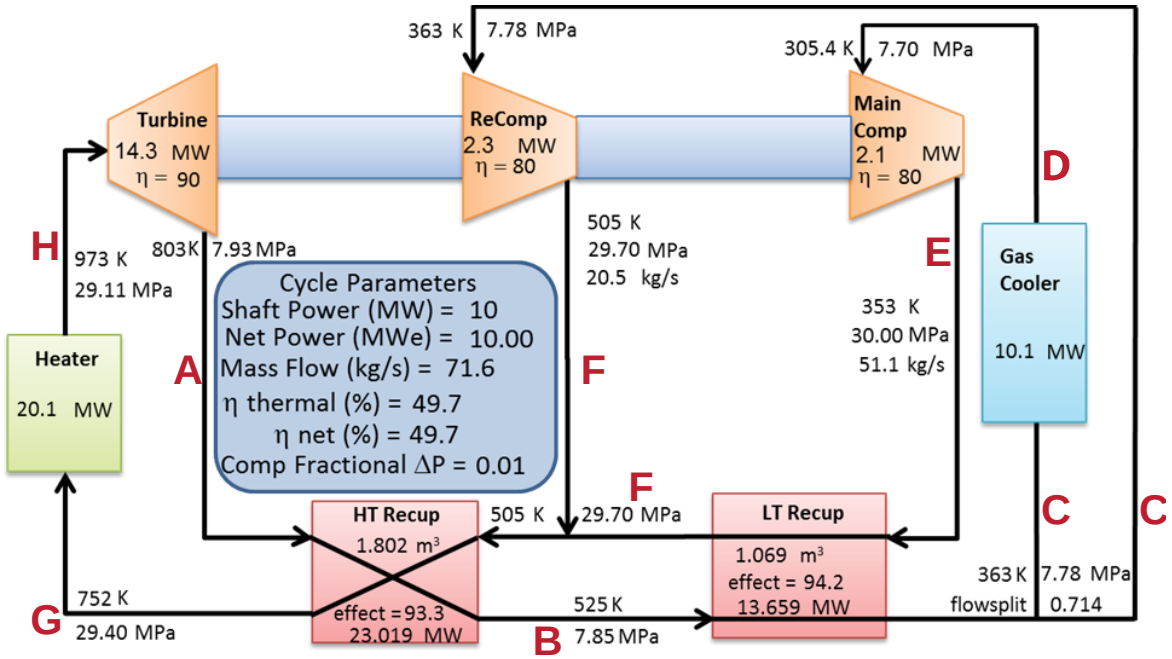

Figure 15. RCBC Flow Sheet for Wet Cooling Conditions, 700°C TIT, at 10 MWe.

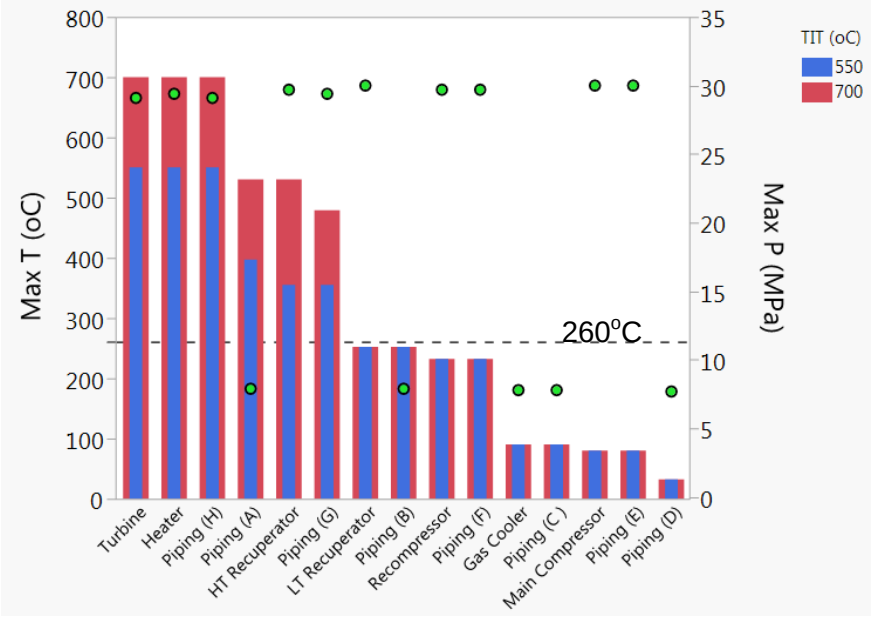

Figure 16. Component temperatures and pressures (green dots) for 550°C and 700°C TIT's.

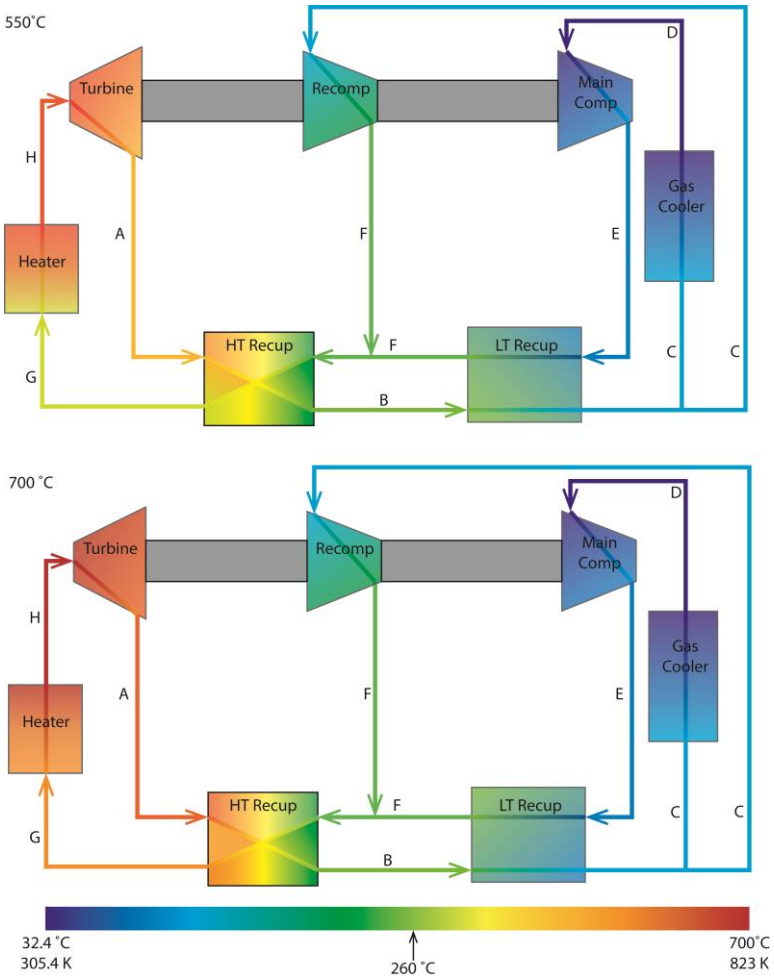

Figure 17. Flow sheet temperature maps for both 500°C and 700°C TIT's.

3.4. Next Steps

Current work in this area is focused on three main areas: 1) Mining for alloy S-CO2 corrosion data (and in some cases for A-USC data where no S-CO2 data is available), 2) the Identification of performance requirements (other than corrosion) for each component and 3) Compiling costs for the range of alloys. Progress along the established process flow diagram is shown in Figure 18. Here, completed tasks and active tasks are indicated by separate markers.

With the completion of the first item, the thickness requirements over the range of alloys will be compiled for each of the components with their specific exposure conditions. For the second item, the next step will be to compile a database of alloy property data for each of the identified performance requirements. Once these are completed, the final portion of this work will be to combine information from these three areas into a single database for facilitating component alloy selection, taking account of both important performance and economic considerations.

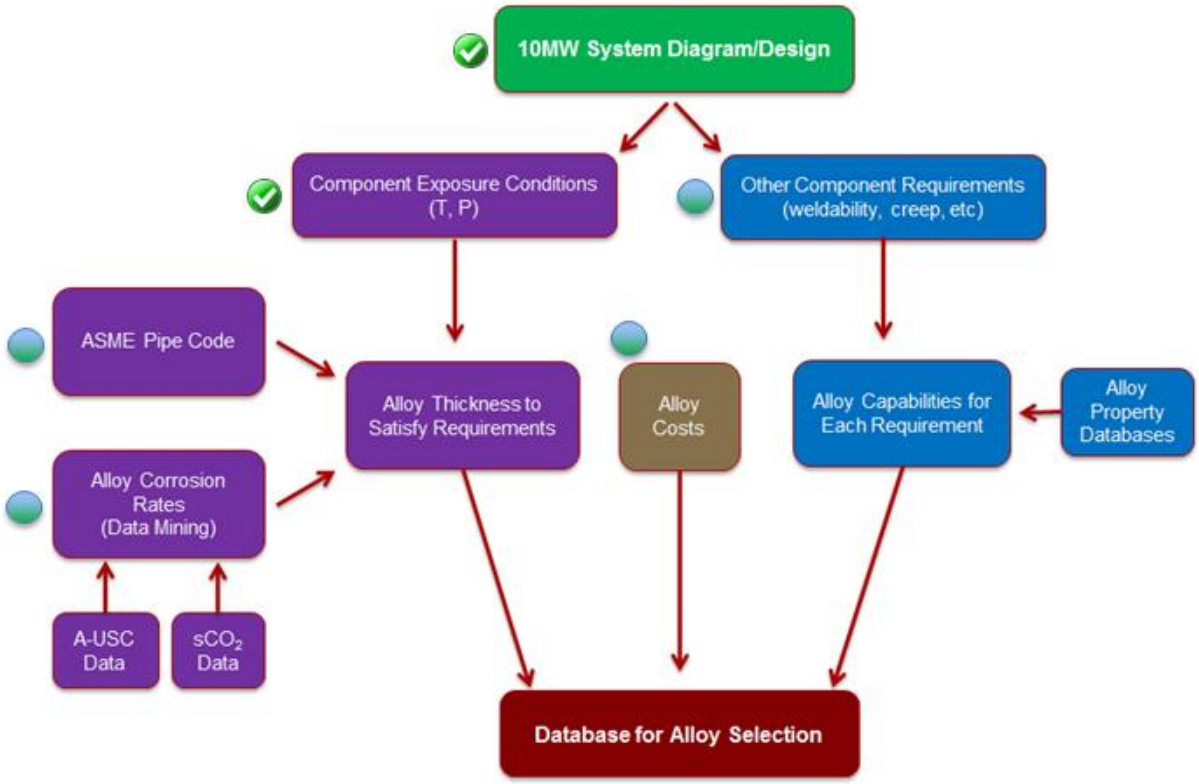

Figure 18. Process flow diagram showing completed (✓) along with active ( ) items.

4. UNDERSTANDING AND RESOLVING TURBINE DEGRADATION

4.1. Background

A consistent observation in the operation of Sandia's S-CO2 RCBC test loop has been turbine degradation. This has only been observed for the turbine and not for the compressor. Also, while it has been observed both for the turbine wheel and turbine nozzle, it has been primarily observed as wear of the turbine nozzle. The alloy in both instances is Alloy 718.

Focusing on the turbine nozzle, two forms of degradation have been observed. One form, shown in Figure 19, is the pitting of nozzle surfaces resulting in a matte surface finish that resembles that of a grit-blasted surface. The other form, shown in Figure 20, involves the thinning and eventually deformation of the thinnest sections of the nozzle.

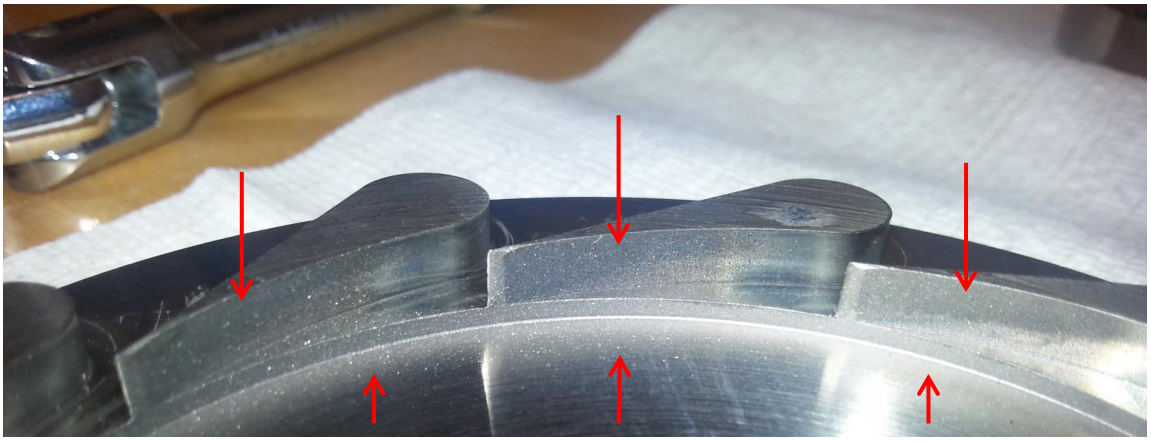

Figure 19. Turbine nozzle showing areas of metal pitting/wear (indicated by arrows).

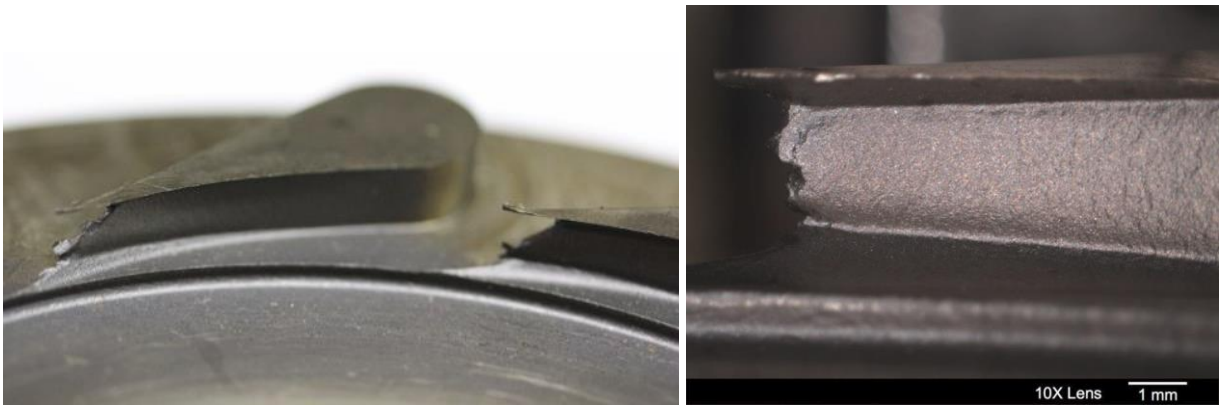

Figure 20. Excessive pitting and wear observed for flow directing portion of a turbine nozzle.

Some analyses have been conducted by Sandia in the past to understand this issue. While these did not identify the specific cause for the observed degradation, they did provide some valuable information. An analysis of the operational regime within the turbine indicated that liquid impingement should never be an issue with S-CO2, and that all wear should be attributed to non-liquid erosion. Microscopic characterization of worn vs. non-worn surfaces indicated significant differences both in terms of appearance as well as chemistry. In Figure 21, SEM images of two separate surfaces are shown at two magnifications. In the case of Surface 2, this is a non-flow surface and one that did not show visible wear. Microscopically this surface appears rather smooth and unchanged during operation in the test loop; machining marks from when the part was made are even evident. Chemical analyses of this surface using Energy Dispersive Spectroscopy (EDS) revealed little change to the surface chemistry versus that for the original alloy. Conversely, Surface 3 is a surface that is the path of flow and one that had visible wear evident by its characteristic matte finish. Now, no machining artifacts were present on the surface, but instead the surface showed increased roughness resembling wear damage. Also, the surface chemistry showed significant iron enrichment versus the original alloy.

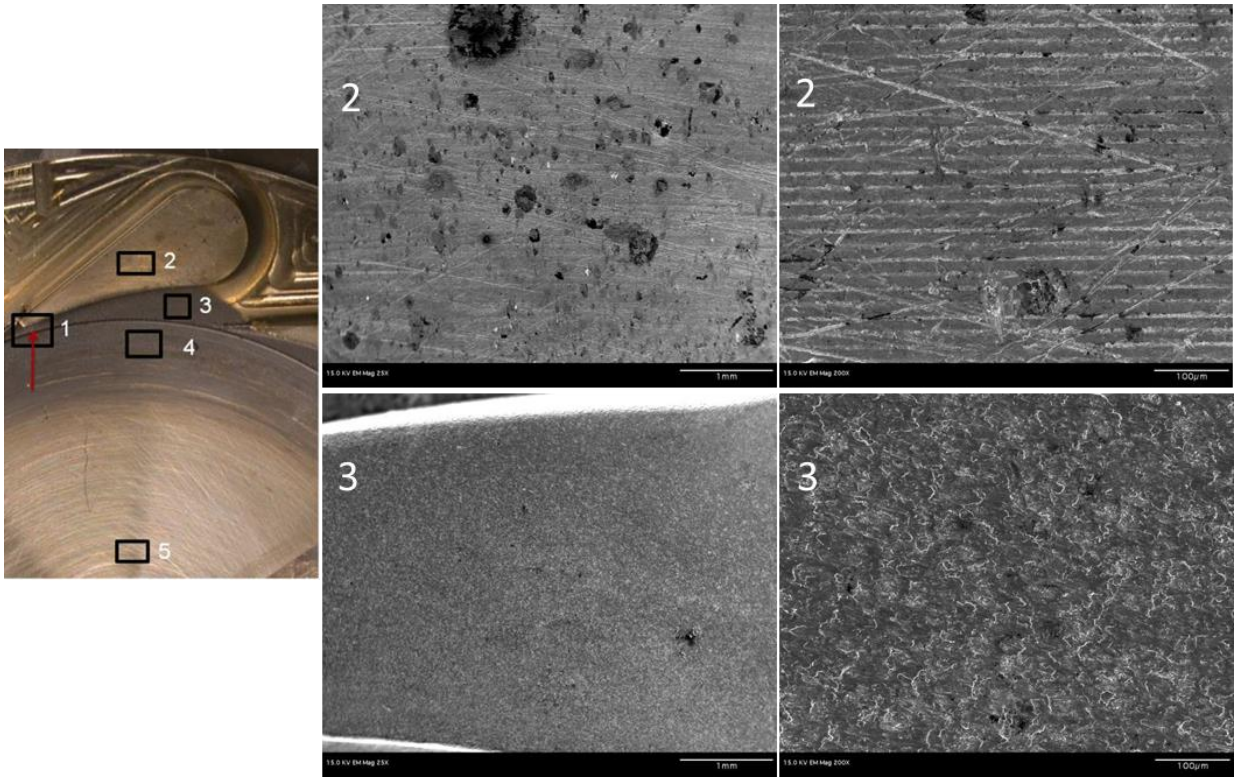

Figure 21. Comparison of a non-flow surface with no wear (2) to a surface in the flow path with evident wear (3).

Based on this information, the cause for the observed wear was believed to be caused by the impingement of iron-rich particles with surfaces in the gas flow path. Furthermore, a hypothesis was developed that the source of these particles was the spallation of iron oxide from the interior walls of carbon steel gas inventory tanks; prior to use in the test loop, hydro pressure testing may have caused internal oxidation within the tanks. Testing was never conducted to prove out this hypothesis. As a result, the specific cause of observed turbine degradation is currently unclear. This presents significant risk to future development of this process if not completely understood and resolved at the smaller scale of the current test system. In order to fully understand and resolve this issue, a detailed failure investigation is being performed. A key element of this is conducting a root cause analysis (RCA) for turbine degradation.

4.2. Approach

The specific process used to conduct this failure investigation was prepared using a valuable resource from ASM International and Daniel P. Dennies titled, *How to Organize and Run a Failure Investigation*[13]. In this book, the author describes a plan for finding the root cause of a particular failure, and to ultimately implement effective corrective actions to eliminate it. Here, the process is applied to resolving an identified problem, turbine degradation, versus necessarily a failure.

The major steps in this process are shown in Figure 22. A team of Sandia contributors across a range of expertise were identified to participate in each step of the process. The first step is to complete a RCA. This is focused on first obtaining a clear understanding of the failure, followed by the identification of all possible root causes in the form of fault tree. Converging on the most likely root cause is the focus of the next two steps. This is done by prioritizing and evaluating the identified root causes in the fault tree. The final three steps involve the identification and implementation of an optimal corrective action to eliminate turbine degradation.

4.3. Results

In February 2016 a team of seven contributors gathered in Albuquerque, New Mexico for two days to complete the first step in the failure investigation process. During the first day, information was presented describing the current state of understanding for turbine degradation. A brainstorming activity during the second day resulted in the creation of a detailed fault tree containing over 60 possible causes across 5 main categories. These categories include Foreign Materials, Turbine Materials, Turbine Design, Process Operations, and Turbine-Alternator-Compressor (TAC) Build; each of the categories along with their identified causes are shown in Figure 23, Figure 24, Figure 25, Figure 26, and Figure 27, respectively.

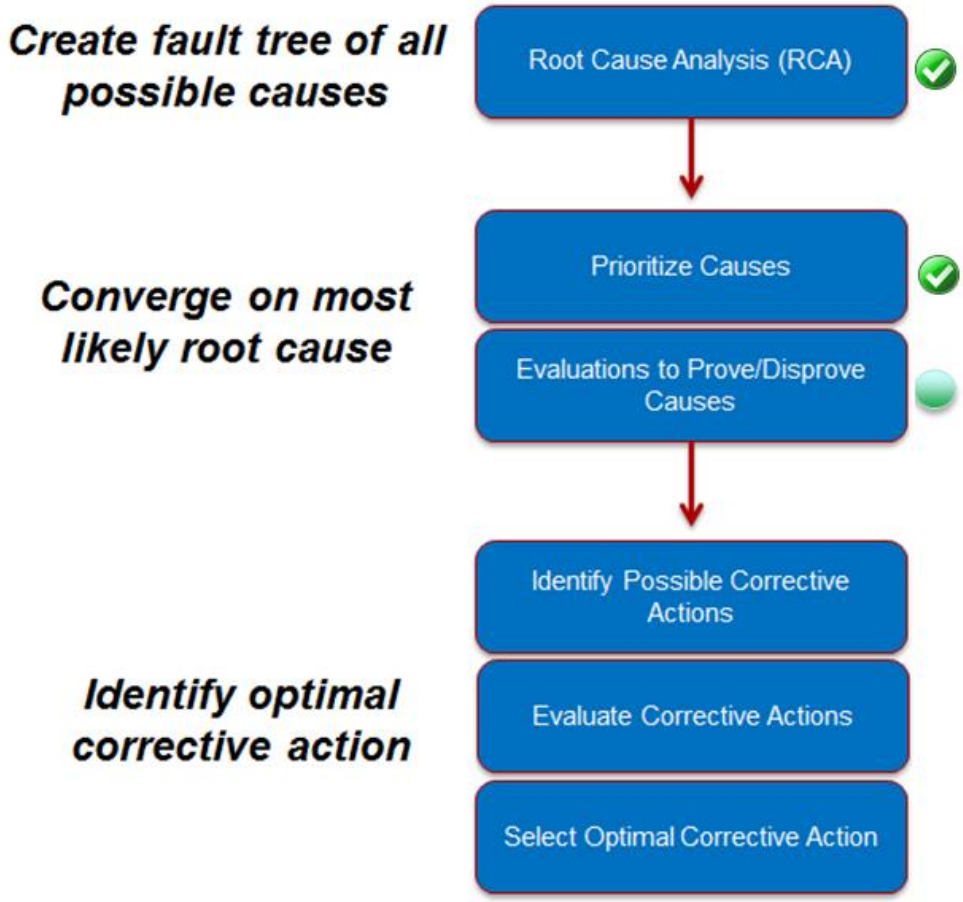

Figure 22. Failure investigation process flow diagram showing completed (✓) along with active ( ) items.

The 60 possible causes in the fault tree are far too many to evaluate in depth. During a subsequent teleconference meeting, the team reconvened to prioritize each of the identified causes using a Failure Mode Assessment (FMA). Here, each of the causes was discussed, ultimately assigning a probability to it along with the rationale for doing so. This resulted in a list of 11 high priority causes across each of the 5 main categories. These are listed in Table 3 as part of a detailed Technical Plan of Resolution (TPR) for evaluating each of these priority causes.

The TPR that was developed includes plans for evaluating each of the high priority causes, along with the individual/s responsible for completing each evaluation. Of these 11 possible causes, plans are established to evaluate 9 causes. The remaining 2 causes, focused around the TAC Build, are viewed as lower priority to the others, and will be evaluated only if the other causes are found to be disproven. The plans for the other 9 causes involve a mixture of experimental and non-experimental evaluations. Experimental evaluations, mainly focused on identifying sources for particles within the loop, will utilize a combination of particulate filters along with

borescope inspection cameras. Areas to investigate include CO_2 bottles, inventory/expansion tanks, heaters, loop interior piping and ports (burrs), and bearing surfaces. Non-experimental evaluations are focused on the turbine materials and turbine design. In both instances, the focus is on working with others (turbine vendor and turbine design shop) to ensure that the materials/design are appropriate for the application, and are not contributing to the degradation that has been observed.

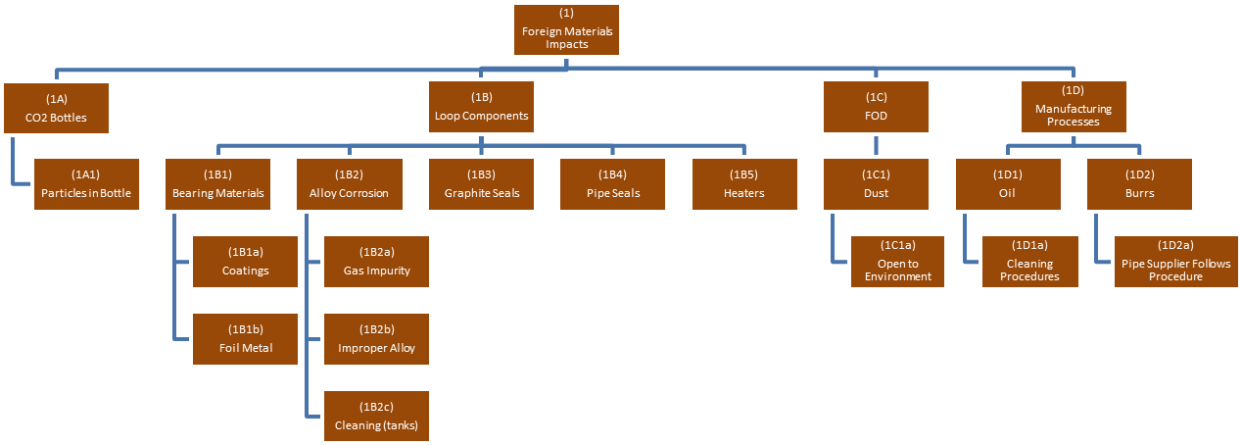

Figure 23. Turbine degradation RCA fault tree branch on Foreign Material Impacts.

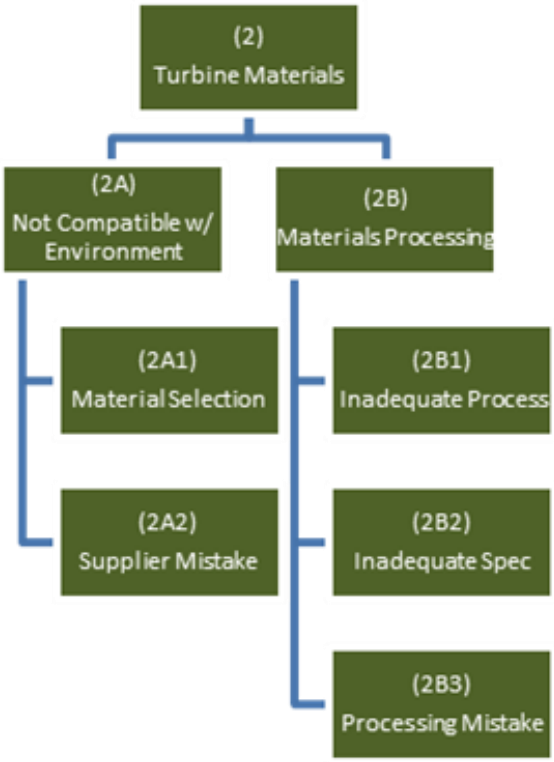

Figure 24. Turbine degradation RCA fault tree branch on Turbine Materials.

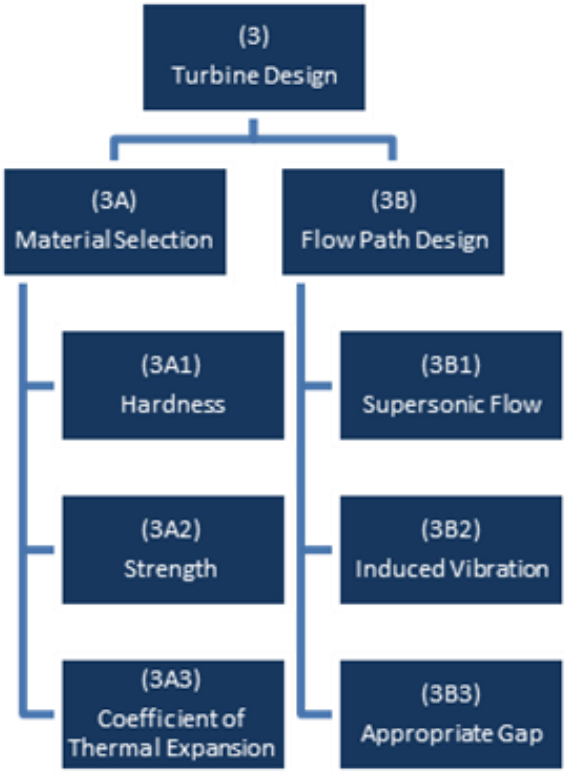

Figure 25. Turbine degradation RCA fault tree branch on Turbine Design.

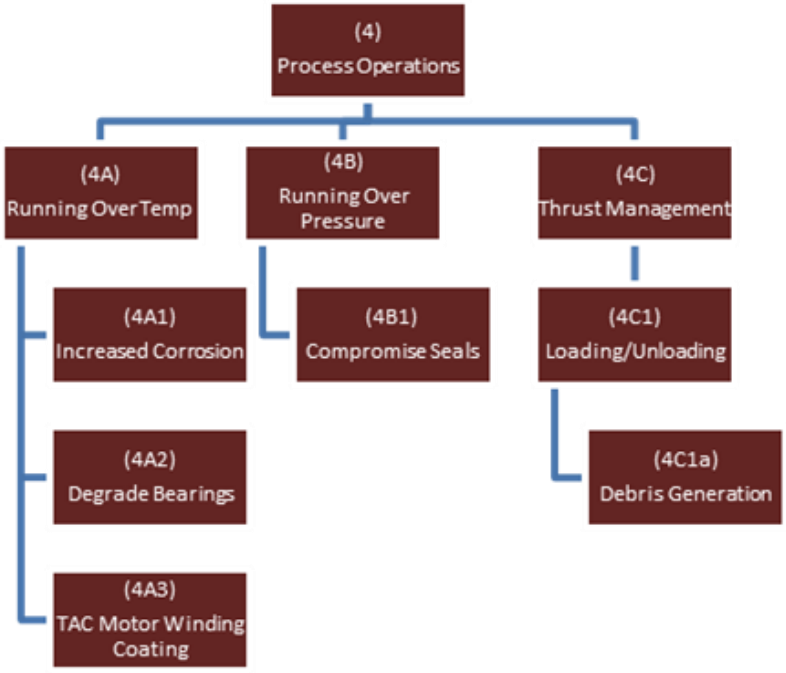

Figure 26. Turbine degradation RCA fault tree branch on Process Operations.

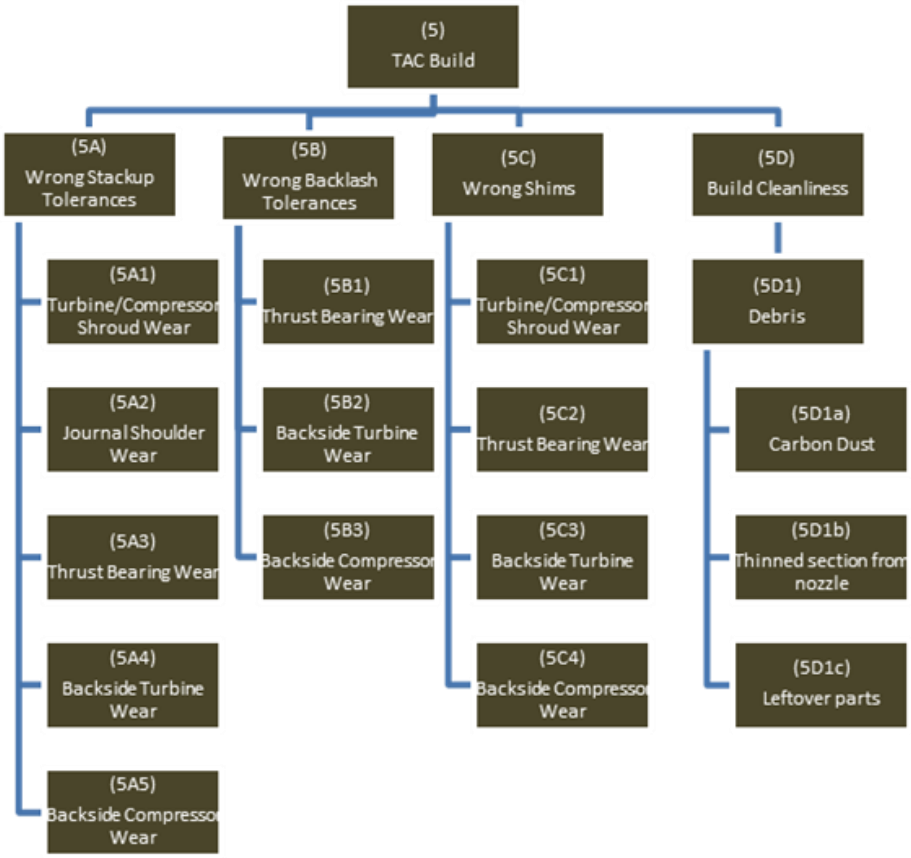

Figure 27. Turbine degradation RCA fault tree branch on TAC Build.

Table 3. Technical Plan of Resolution for Identifying the Root Cause for Turbine Degradation

Item #	Main Category	Sub Category	Potential Root Cause	Rationale	Plan for Proving/Disproving	Key Elements	Owners
1	Foreign Materials Impacts	CO2 Bottles	Particles in Bottle	gas siphoned from bottom of bottle, may pull in particles	Can add filter to exit line from bottles, but concerned over pressure drop. Other concern is that not all bottles may have particles. Solution is an offline experiment where multiple gas bottles (~ 6) are blown down through a filter that is installed. Post-blowdown the filter is checked for particles. Need to find a filter for this.	(1) Offline Experiment using Filter	Fleming,Sharpe, Walker
2	Foreign Materials Impacts	Loop Components	Expansion Tank Corrosion	tanks have not been cleaned since SNL	Two ideas were discussed. One is to take a tank off-line and to pig it out, checking for and detecting loose particles on the tank interior. The second option, and more preferable starting point, is to first do an offline experiment where a filter is installed at the exit from the expansion tanks. This experiment would be combined with the CO2 bottles experiments, where the expansion tanks would be filled and then evacuated into the filter that is installed. If particles are detected in the filter during this test, then one of the tanks would be taken out and pigged to check for particles.	(1) Boroscope Inspection. (2) Offline Experiment using Filter	Fleming,Sharpe, Walker
3	Foreign Materials Impacts	Loop Components	Heater Corrosion	never looked inside	Start with a boroscope inspection of the inside of steel shells around the heating elements. The goal here is to check for what appear to be loose particles inside of these shells on shell walls or heating elements themselves. If nothing is found here, then eliminate this as a possibility and move on to others. If corrosion appears evident, then do an offline experiment where a filter is installed at the exit of the heater section, and a slow flow of gas is passed in through the heaters to this filter.	(1) Boroscope Inspection. (2) Offline Experiment using Filter	Fleming,Sharpe, Walker
4	Foreign Materials Impacts	Loop Components	Burrs	we have found burrs	Use the boroscope to do a complete loop inspection for burrs. If there are no burrs identified, then eliminate as a cause since we still are seeing turbine degradation in the absence of burrs. If burrs are present, then we need to go in and smooth these out, and then see how this may influence turbine degradation on future test loop runs.	(1) Boroscope Inspection	Fleming,Sharpe, Walker
5	Turbine Materials		Supplier Mistake	Not sure about current processing of 718 parts, or if these can impact hardness of completed parts.	It seems that this may have already been adressed by the turbine vendor. Need to verify and understand their record keeping process.	No experimental work	Kruizenga, Walker
6	Turbine Materials		Inadequate Process	hardness of completed parts.	Understand turbine materials processing steps. Understand how materials hardness is affected by these.	No experimental work	Kruizenga, Walker
7	Turbine Design	Materials Selection	Coefficient of Thermal Expansion	seen this before just did analysis there are thermal growth issues	This will be rolled into work with Concepts NRC --- They will look over our design and run thermal analyses to ensure that thermal growth is not an issue and that we have proper clearance with current materials and flow path design	No experimental work	Fleming
8	Turbine Design	Flow Path Design	Appropriate Gap	very possible due to dissimiliar materials with thermal growth	This will be rolled into work with Concepts NRC --- They will look over our design and run thermal analyses to ensure that thermal growth is not an issue and that we have proper clearance with current materials and flow path design	No experimental work	Fleming
9	Process Operation	Thrust Management	Loading/Unloading	we do have thrust problems	Start with an inspection of all bearing surfaces for wear. All particles generated during thrust issues would pass through to the hydropac. So, the second step is to inspect the hydropac cylinder walls for wear/erosion. Use boroscope for this?	(1) Visual bearing inspection (2) Boroscope inspection of hydropac cylinder walls	Fleming,Sharpe, Walker
10	TAC Build	Turbine/Compressor Shroud Wear	Wrong Stackup Tolerances	we have had this before when building	We are going to wait on these for now. We will move to these if we have completed Items 1-9 without identification of the root cause for Turbine Degradation		
11	TAC Build	Turbine/Compressor Shroud Wear	Wrong Shims	we have seen this			

4.4. Next Steps

The next step in resolving turbine degradation is to complete each of the TPR evaluations. Plans are in place to complete each of these evaluations in June 2016. Two possible scenarios following these evaluations are: (1) One or more of the causes is found to contribute to turbine degradation, or conversely (2) none of the causes is found to contribute. In the first scenario, activity shifts to finding optimal corrective actions that can be implemented to prevent future turbine degradation, and then work concludes after the corrective actions have been verified as effective. In the second scenario, activity shifts back to the fault tree and FMA to identify other causes that could be evaluated for a causal relationship to turbine degradation.

PAGE INTENTIONALLY LEFT BLANK

5. IDENTIFYING GAS FOIL BEARING BEHAVIOR IN CO_2

5.1. Background

The Sandia S-CO2 RCBC loop TAC utilizes a series of bearings. Radial (or Journal) bearings are located at both the turbine and compressor sides of the TAC, while the compressor side also has a thrust bearing. The locations for each bearing are shown in Figure 28. In Sandia's loop, each bearing operates in an environment of around 300 psi CO_2. The turbine-side radial bearing is at a significantly higher temperature (~550^{o}C) than at either of the compressor-side bearings (~ 315^{o}C).

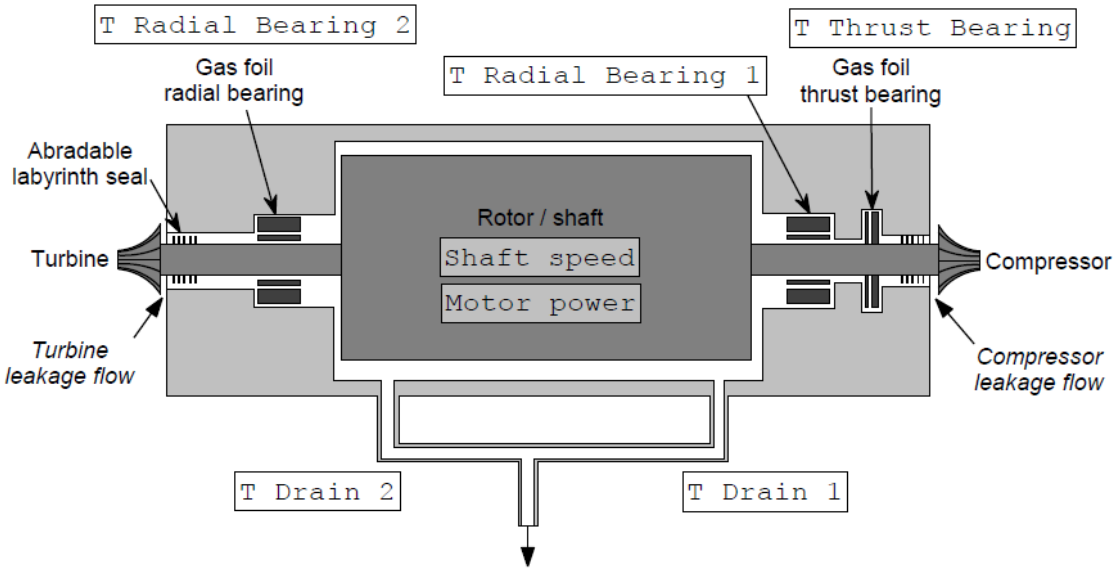

Figure 28. Diagram of Sandia's S-CO2 loop TAC showing the location for the bearings.

All bearings in this TAC are gas foil bearing. Metal foil sections (typically Alloy x750) line the interior of these bearings. Images of a gas foil radial bearing are shown in Figure 29, while one for a gas foil thrust bearing is shown in Figure 30. At high shaft rotational speed these bearings allow for the shaft to ride on a cushion of air. Conversely, at lower speeds during startup and shutdown, the shaft rides along the foil itself. The outer metal foils have low-friction coatings on their outer surfaces in order to facilitate rotation during these periods. During the design of the Sandia TAC, different temperatures across the TAC resulted in different coatings being used for turbine-side and compressor-side foil bearings. A lower temperature Teflon based coating is used for the compressor-side bearings, while a higher temperature coating was used for the turbine-side bearing. The turbine-side radial bearing, being developed by an outside vendor (Capstone Turbines) utilizes a proprietary coating of unknown chemistry.

Information regarding the performance of these bearings has been gleaned through their operation in the Sandia S-CO2 RCBC during the past several years. The journal bearings have appeared to work adequately; while there have been challenges with the thrust bearing. Consensus is that the Teflon coating appears inadequate for the temperatures in which this bearing operates. Actually very little is known about the behavior of all coated foils in the high

temperature/pressure environment of these bearings. This information is valuable to understanding and optimizing gas foil bearings for this system, as the coating performance cannot currently be separated from current issues.

Two areas of research at Sandia will address this. One is the establishment of a separate rig for conducting bearing tests. Once commissioned, this will be used for evaluating vendor supplied bearing performance under conditions relevant to S-CO2 RCBC operation. The other area is the evaluation of foil coatings themselves in relevant pressure/temperature environments. These will be valuable in screening vendor supplied foils for use in future gas foil bearing rig tests, in addition to providing a baseline of behavior for the currently used foils.

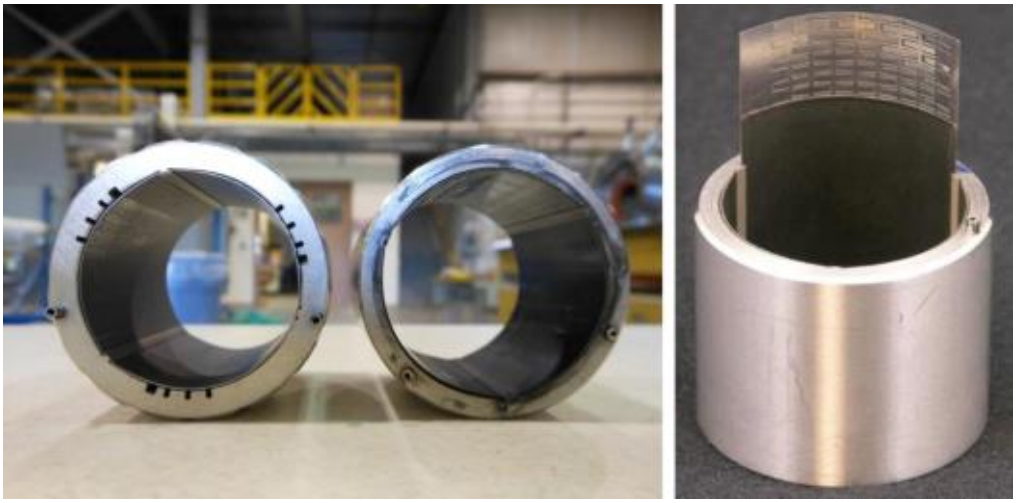

Figure 29. Images of the gas foil radial (journal) bearings used in Sandia's S-CO2 RCBC loop.

Figure 30. Images of the gas foil thrust bearing used in Sandia's S-CO2 RCBC loop.

5.2. Approach

The overall approach involves working with bearing vendors to receive coated foil samples that will be tested in relevant temperature and pressure conditions to the bearings within the Sandia TAC. Post-exposed samples will be characterized to understand behavior in this environment. This information will be utilized in selecting foil bearing coatings to be used in future bearing rig tests.

Three key elements to this approach are as follows: (1) Engage bearing vendors who have interest in providing samples for these tests, (2) Develop/Setup an appropriate test configuration for completing these evaluations, and (3) Identify sample characterizations for test samples that are important to coated foil within an S-CO2 RCBC gas foil bearing.

5.3. Results

Three separate vendors expressed interest in providing samples for these tests: Mohawk Innovative Technologies, Xdot Engineering and Analysis, and Mechanical Solutions, Inc. Bearing temperature and pressure conditions were provided to each vendor, and they each made determination for the appropriate coating to provide on their foil test samples. Inclusion of samples that have the current coatings used in Sandia's test loop bearings is important as a comparison to the vendor supplied samples. Only samples with the lower temperature compressor-side bearing coating will be included, as the supplier for the other bearings (Capstone Turbines) was unwilling to provide samples for these tests.

Mohawk Innovative Technologies will provide one type of coated samples for these tests. Mechanical Solutions, inc. is providing samples with three different types of coatings, while Xdot Engineering and Analysis is providing samples with 4-5 different types of coatings. All coatings will be evaluated at both temperatures. All of the samples required for these tests have not been received from the vendors. Two of the vendors (Mohawk and Mechanical Solutions) have requested that an Non-Disclosure Agreement (NDA) be setup to protect their coating chemistry. Draft NDA's have been sent to both vendors for their signatures.

The testing plan that has been established for these evaluations is shown in Table 4. The plan is to conduct one 2000 hour test at each of the temperatures. Each vendor will provide sufficient samples enabling characterization at 500 hour intervals up to a max of 2000 hours for each of the two test temperatures. One of each type of sample will be characterized prior to exposure, providing a baseline to compare against exposed samples of the same variety.

Table 4. Testing Plan for Vendor Supplied Bearing Foil Materials in CO_2

Source	Temperature, °C	Pressure, psi	Duration, hrs
Mohawk Innovative Technologies	315, 550	300	500, 1000, 1500, 2000
Xdot Engineering and Analysis			
Mechanical Solutions, Inc.			
Baseline (Thrust only)			

The test configuration for these evaluations has been established. The autoclave furnace that was shown in Figure 3 will be used. This furnace will require slight modification enabling tests at 300 psi CO_2. Also, a new sample holder will be designed/fabricated for use in these experiments. At this time, neither of these items has been completed.

Appropriate pre- and post-exposure sample characterizations have been identified. The microstructure of the base metal plus coating will be evaluated for samples at each time interval (including pre-exposure). Measurements will also be made for coating adhesion strength and coating surface roughness for samples at each interval. Performance of each coating in these three areas will be valuable in selecting appropriate coatings for more advanced future bearing rig tests, which will include cyclical start-stop testing to get at tribological properties (i.e. friction).

5.4. Next Steps

The test setup modification and samples holder design/fabrication need to be completed prior to starting testing. The target for completing both of these is the end of June. An NDA needs to be finalized with both Mohawk and Mechanical Solutions prior to receiving their test samples. Also, while the appropriate sample characterizations have been identified, the specific tests for completing these needs to be identified. Specific tests for coating surface adhesion and coating surface roughness need to be identified, as multiple approaches exist to these measurements. The target for completing both of these is the middle of June.

The current schedule projects that the first of two 2000 hour tests (~ 83 days) will start in early July, completing the full 2000 hours around the middle of September. Analyses performed on samples from this test at 500 hour intervals, will provide data for exposure less than 2000 hours for the final report at the end of August. Data will not be available from the second 2000 hour test prior to this final report, as this test will not start until around the middle of September.

6. IDENTIFYING GAS CHEMISTRY INFLUENCE ON ALLOY CORROSION

6.1. Background

For S-CO2 induced material corrosion, a critical shortcoming in the available experimental data is that high purity CO_2 (research grade - 99.999% purity) has exclusively been used in these studies, while a commercial scale system is likely to use industrial grade CO_2 with higher impurity concentrations (~99.5% purity). So, while the corrosion of some materials is well understood in a high purity CO_2 environment, this environment is never likely to be present in a commercial scale system. Instead, it is likely to contain impurities common to industrial grade gases (CO, O_2, H_2O, H_2, N_2, CH_4, etc.) as well as other contaminant gas species resulting from component outgassing and/or surface contaminants from within the RCBC system. A critical need exists in understanding how the composition (impurity concentration) of the CO_2 used in the system can change during operation, as well as how these impurities, along with those already present in the industrial grade gas, will impact the corrosion of the materials used.

Some recent experimental work by others (ORNL[14], NETL[15], and Wisconsin[16]) has been initiated to understand the impact of gas chemistry on alloy corrosion. This work is focused on the higher temperatures (>650^{o}C) used in fossil and solar heated S-CO2 systems, and it also only looks at a very limited set of gas impurity concentrations. Alloy corrosion behavior in these gas chemistries may change in moving to the lower temperatures used in a nuclear energy heated system. Also, the range of gas chemistries needs to be expanded beyond this limited set. A combination of approaches are used as part of this work at Sandia to both achieve the necessary experimental low temperature alloy corrosion data, as well as expanding the range of gas chemistries examined through the use of modelling techniques.

6.2. Approach

In developing the necessary understanding for gas chemistry influence on alloy corrosion, Sandia's approach includes the combination of the following three items: (1) Alloy corrosion experiments in gases with different impurity concentrations, (2) Thermochemical modelling of gas-alloy interactions, and (3) Molecular Dynamics modelling and simulations of interfacial processes. This is illustrated schematically in Figure 31. The introduction of the two modelling components are unique to the approaches used by other groups, and have the capability of bringing tremendous value to this effort. In particular, the fundamental understanding that these provide for the corrosion mechanisms and how these change over a range of gas chemistries, should enable understanding across a much wider range of conditions (gas chemistry and temperature) than experimental techniques can provide in a reasonable timeframe.

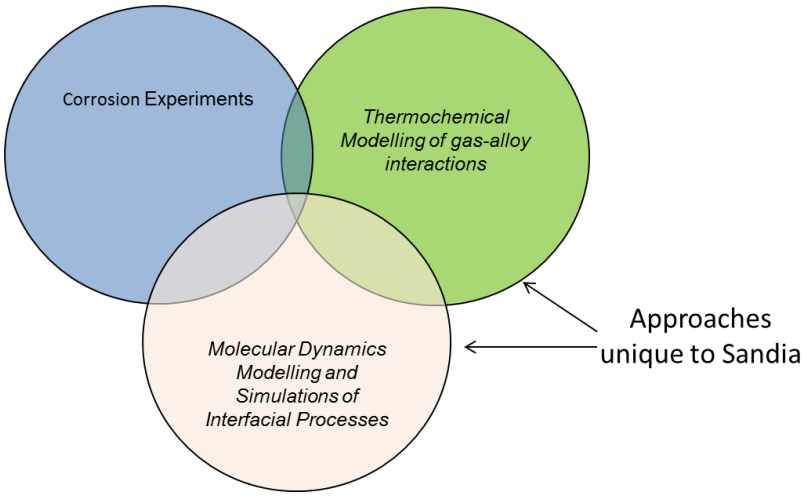

Figure 31. Three components of Sandia's approach to alloy corrosion understanding.

6.2.1. Corrosion Experiments

Two large tube furnaces (3ft length) are being setup to complete the alloy corrosion experiments at Sandia's laboratory in Livermore, CA. These experiments will be conducted at atmospheric CO_2 pressure, as recent results from others[19] indicates that CO_2 gas pressure does not appear to influence alloy corrosion. All experiments will be completed over a 2000 hour duration at 550°C, using alloys from across the corrosion performance (and cost) spectrum (Inconel 625, 316 stainless, HR120, and Grade 91 alloy). Similarly to other experiments, samples of each alloy will be pulled and analyzed for corrosion at 500 hour intervals. Initial experiments will involve the use of two gas chemistries, covering the full range of expected gas impurities from the highest purity (research grade – 99.999%) to the lowest purity (industrial grade – 99.5%). Subsequent experiments will isolate each gas impurity separately (at 0.5% concentration in CO_2) to understand its influence on corrosion. Each of the gas chemistries that will be explored through these experiments are shown in Table 5.

Table 5. Gas Chemistries used for Alloy Corrosion Experiments

CO_2	CO	O_2	H_2O	H_2	CH_4
Research Grade 99.999%	< 2ppm	< 2ppm	< 1ppm	< 2ppm	< 4ppm
Industrial Grade 99.5% *	A	B	C	D	E
99.5%	0.5%				
99.5%		0.5%			
99.5%			0.5%		
99.5%				0.5%	
99.5%					0.5%

* Need to measure gas for specific impurity concentrations

6.2.2. Thermochemical Modelling

Understanding thermochemical interactions at alloy-gas interfaces provides valuable information regarding the equilibrium surface phases as functions of alloy chemistry, gas chemistry, and temperature. The surface phases which form may influence corrosion of the base alloy, and so it is important to understand and predict these interactions. As an example, calculated oxide scale formations (chemistry and phase) in a steel alloy under different oxygen partial pressures at constant temperature (900°C) are shown in Figure 32. Predictions can be made using thermochemical computer programs. Two common programs are Thermo-Calc and FactSage. The calculations in Figure 32 were done using Thermo-Calc. FactSage will be used in place of Thermo-Calc for this work due to its more extensive oxide phase database.

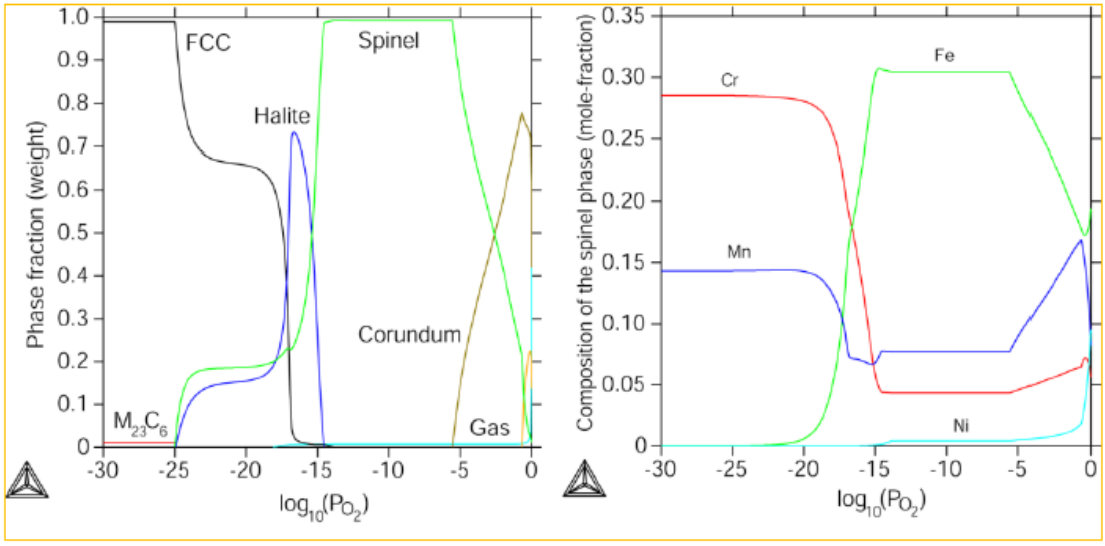

Figure 32. Thermo-Calc calculated oxide scale formations in a Fe-Mn-Cr-Ni-C steel under various partial pressures and a constant 900°C.

6.2.3. Molecular Dynamics Modelling and Simulation

Ab-initio molecular dynamics (AIMD) simulations will be carried out using Vienna Ab-initio Simulation Package (VASP) software to reveal important carburization and corrosion mechanisms along with the underlying thermodynamics of these processes. Density functional theory (DFT) will obtain Raman signatures for direct comparison with experiments. Outputs from these models will be activation energies that can be compared to experimental data. Validated models will provide insight into molecular behavior that will aide interpretation of experimental results; this is a natural validation and verification approach to promote confidence in the final conclusions.

One portion of the associated experimental work includes Electron Backscatter Diffraction (EBSD) of pure Ni and Fe sample surfaces to determine the major crystallographic orientations and other surface properties. A second portion of the experimental work involves 500 hour exposure test of these same high purity Fe and Ni samples in atmospheric pressure CO_2 at both 700K (427^{o}C) and 850K (577^{o}C). Results from both types of experiments will be invaluable to robust model development

6.3. Results

6.3.1. Corrosion Experiments

A test plan has been developed for these experiments, including the alloys, gas chemistries, temperature, and time durations to be evaluated. Alloy samples are being prepared for these experiments, and the necessary gases are being ordered. The installation of the tube furnaces for these experiments has started but is not yet completed.

6.3.2. Thermochemical Modelling

The thermochemical modelling software package for completing this work, FactSage, has been ordered and delivered to Sandia in Livermore, CA. Initial work has focused on the creation of predominance area diagrams for the exploration of equilibrium alloy surface phases across a range of gas chemistries. Here, gas chemistries are represented by their respective oxygen partial pressure (pO_2) and carbon activity (a_C). This has been done for pure Fe as well as for Fe-Cr.

In the case of the pure Fe system, the predominance area diagram was examined at three temperatures (800, 850, and 900K) to understand how equilibrium surface phase may change over this range. The diagram produced by this work is shown in Figure 33. For the Fe-Cr system, the predominance area diagram was examined at a single temperature (850K). The diagram produced by this work is shown in Figure 34. Both diagrams provide valuable information regarding the transition between stable surface oxides across the range of gas pO_2 and temperature. The rate of corrosion may be dependent upon the surface phase that forms on an alloy, and understanding the impact of gas chemistry and temperature on this would be valuable here. In both instances, it is important to validate the predictions in these diagrams against experimental corrosion data. Here, validation will provide confidence in the use of these diagrams for making engineering decisions regarding alloy selections and gas chemistry optimization.

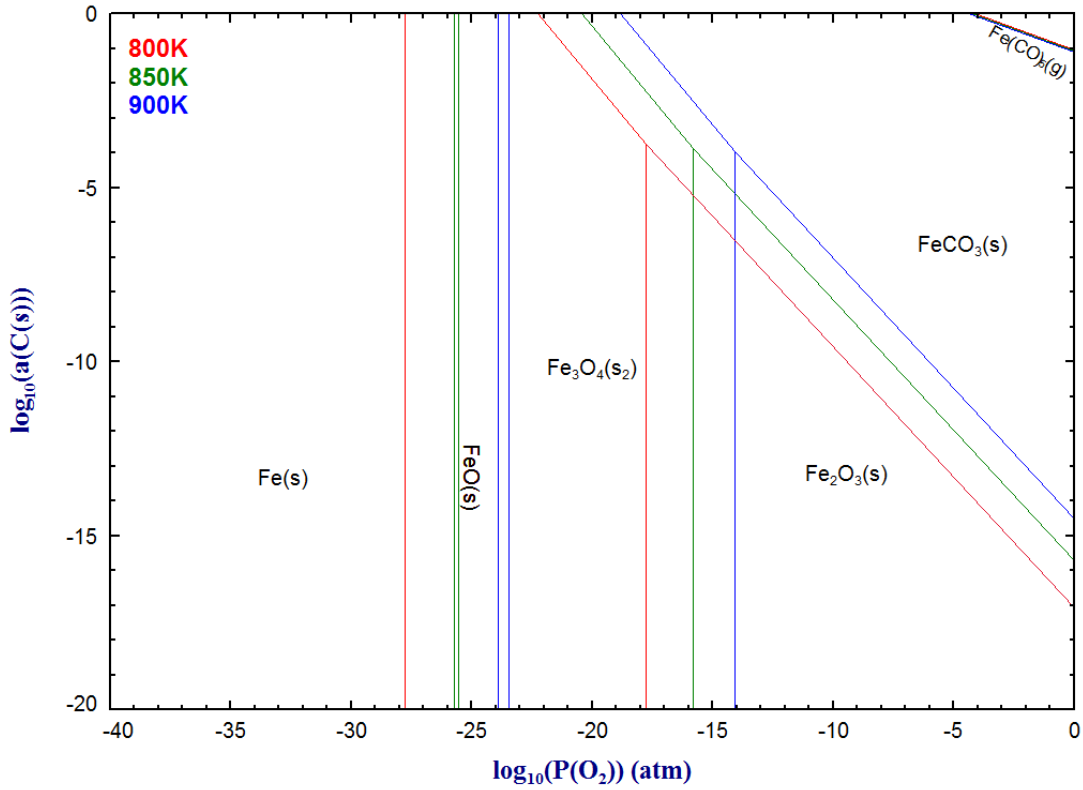

Figure 33. Predominance area diagram for pure Fe at 3 T's across range of gas pO_2 & a_C.

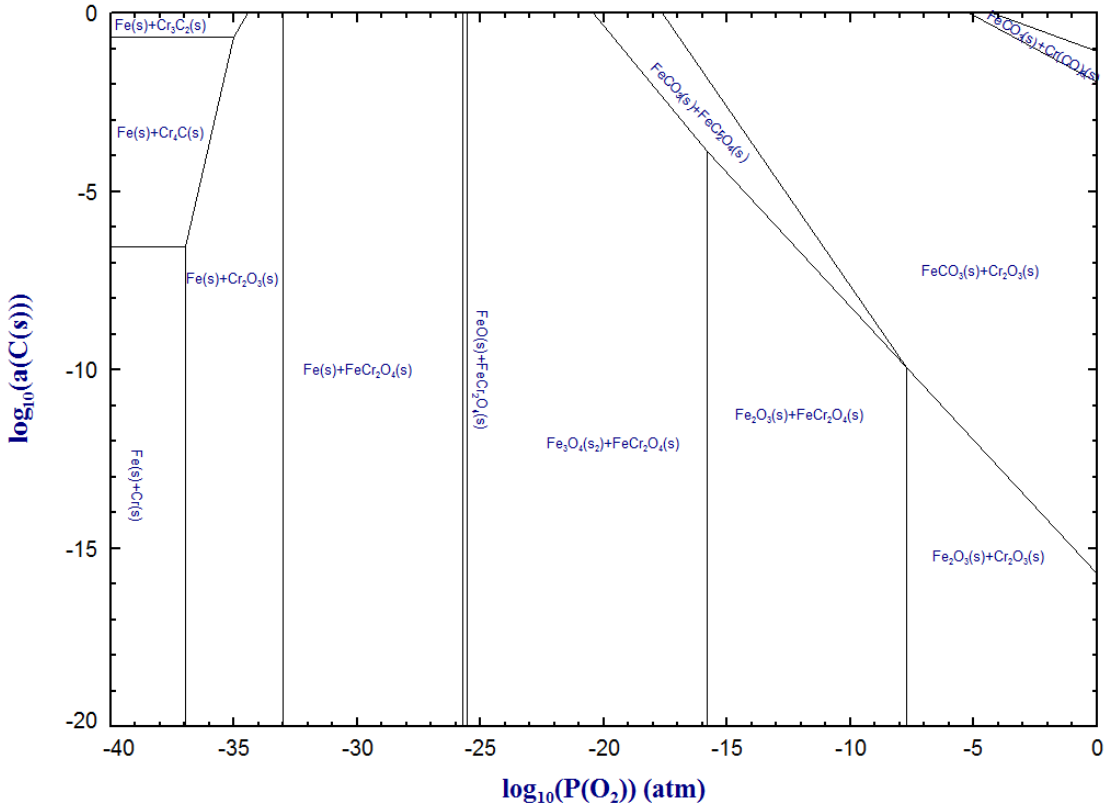

Figure 34. Predominance area diagram for Fe-Cr at 850K across a range of gas pO_2 & a_C.

6.3.3. Molecular Dynamics Modelling and Simulation

Complementing the experimental work (including EBSD of pure Ni and Fe surfaces to determine major crystallographic orientations and other surface properties), atomistic models of Fe and Ni bulk and low-index surfaces were built in order to analyze experimental observations and predict structural trends upon surface exposure to CO_2.

First-principles calculations were performed using spin-polarized density functional theory (DFT) as implemented in the Vienna *ab initio* simulation package (VASP) [18]. The exchange-correlation energy was calculated within the generalized gradient approximation [19] (GGA+*U*), with the parameterization of Perdew, Burke, and Ernzerhof [20] (PBE), corrected with an effective Hubbard parameter +*U* = 0.7 eV to account for the strong on-site Coloumb repulsion between localized Fe 3*d* electrons; for Ni calculations, standard GGA was used (i.e. +*U* = 0.0 eV). Previous studies of Fe bulk and nanostructures using standard functionals, such as the PBE functional, have shown this functional to correctly describe the geometric parameters and properties observed experimentally [21]. In calculations on Fe models, the rotationally-invariant formalism developed by Dudarev and co-workers [22] was used, which consists in adding a penalty functional to the standard GGA total-energy functional, E_{GGA}, that forces the on-site occupancy matrix in the direction of idempotency, i.e.

$$E_{\mathrm{GGA}+U} = E_{\mathrm{GGA}} + \frac{(\bar{U} - \bar{J})}{2} \sum_{\sigma} [\mathrm{Tr}(\rho^{\sigma}) - \mathrm{Tr}(\rho^{\sigma}\rho^{\sigma})]$$

where $\bar{U}$ and $\bar{J}$ are the spherically-averaged matrix elements of the screened electron-electron Coloumb and exchange interactions, respectively, and ρ^{σ} is the density matrix of Fe 3*d* electrons with a given projection of spin σ. In Dudarev's approach only $U_{\mathrm{eff}} = \bar{U} - \bar{J}$ is meaningful. Therefore, only $\bar{U}$ was allowed to vary in the calculations.

The interaction between valence electrons and ionic cores was described by the projector augmented wave (PAW) method [23] [24]. The Fe($4s^2$,$3d^6$), Ni($4s^2$,$3d^6$), C($2s^2$,$2p^2$) and O($2s^2$,$2p^4$) electrons were treated explicitly as valence electrons in the Kohn-Sham (KS) equations and the remaining core electrons together with the nuclei were represented by PAW pseudopotentials. The KS equation was solved using the blocked Davidson [25] iterative matrix diagonalization scheme followed by the residual vector minimization method. The plane-wave cutoff energy for the electronic wavefunctions was set to a value of 500 eV, ensuring the total energy of the system to be converged to within 1 meV/atom. Electronic relaxation was performed with the conjugate gradient method accelerated using the Methfessel-Paxton Fermi-level smearing [26] with a Gaussian width of 0.1 eV.

Ionic relaxation calculations utilized a periodic unit cell approach, without symmetry constraints imposed. Bulk relaxation calculations were first carried out using the quasi-Newton algorithm

and the Hellmann-Feynman forces acting on atoms were converged within 0.01 eV/Å. The Monkhorst-Pack *k*-point scheme [27], with *k*-point meshes of 11×11×11 for bulk body-centered cubic (BCC) Fe and face-centered cubic (FCC) Ni and 5×5×1 for Fe(100) and Ni(100) crystal surface slabs, was utilized for integration in the Brillouin zone (BZ). Bulk structures resulting from total-energy minimization were further relaxed with respect to Hellmann-Feynman forces until a convergence tolerance of 1 meV/Å was reached. Ferromagnetic arrangements of the spins were used in Fe and Ni systems. The optimized lattice parameters of bulk Fe and Ni were 2.87 and 3.52 Å, respectively. The (2✕2) Fe(100) and Ni(100) crystal surface slabs were built from optimized Fe and Ni bulk structures, with 10 Å vacuum separating successive 5-layer thick slabs (cf. Figure 35).

Ab initio molecular dynamics (AIMD) simulations were carried out using DFT with Mermin's generalization to finite temperatures, as implemented in the VASP software. The phase space was sampled by carrying out AIMD simulations with fixed number of atoms, volume and temperature (NVT) for isotherms between 300 and 800 K, by steps of 100 K. The time step for ion-motion was set to 0.7 fs, with velocities scaled at each simulation step to the temperature, and each NVT simulation was run for up to ~4 ps. The bottom of the slabs were passivated by hydrogen atoms in AIMD simulations.

Representative AIMD simulations for pure CO_2 interacting with (2✕2) Fe(100) and Ni(100) slabs at 300 K and 800 K are shown in Figure 36. Ab initio molecular dynamics simulations of pure CO_2 interacting with a (2✕2) Fe(100) slab at (a) 300 K and (b) 800 K and with a (2✕2) Ni(100) slab at (c) 300 K and (b) 800 K. Color legend: Fe, orange; Ni, green; C, grey; O, red; H, white.

No significant effect of temperature were observed from 300 K to 800 K within the simulation time for both Fe and Ni slabs. The top layer of the Fe slab appears more distorted by chemisorption of C/O compared to the Ni slab, and C adatoms on the Fe(100) slab are systematically closer to the surface than O; this might indicate a propensity to carburization in Fe(100) relative to oxide formation.

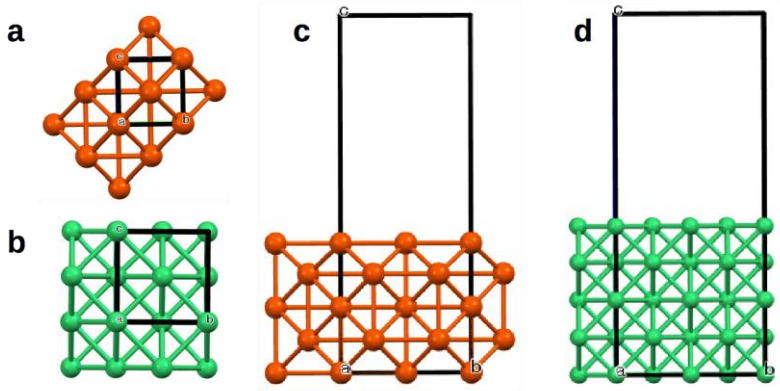

Figure 35. Crystal unit cells of (a) bulk BCC Fe and (b) bulk FCC Ni, and (c) (2×2) Fe(100) and (d) (2×2) Ni(100) crystal surface slabs optimized with DFT at the GGA/PBE level of theory.

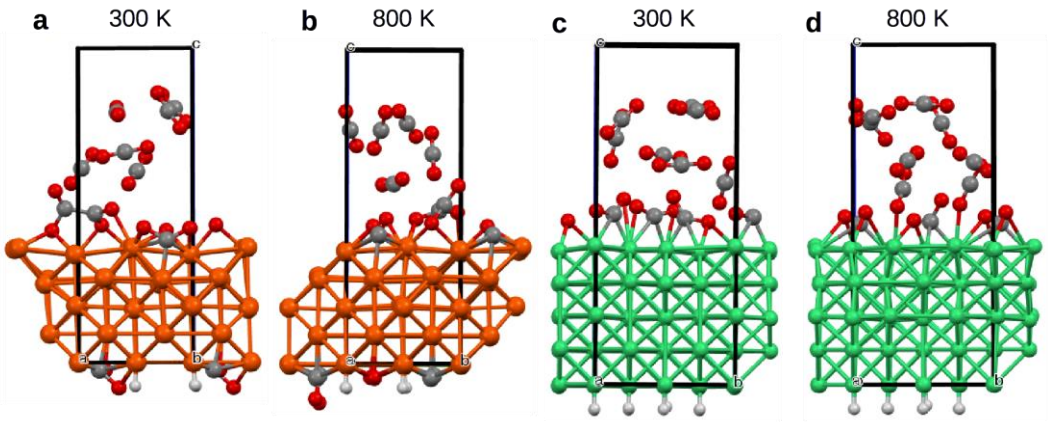

Figure 36. Ab initio molecular dynamics simulations of pure CO_2 interacting with a (2×2) Fe(100) slab at (a) 300 K and (b) 800 K and with a (2×2) Ni(100) slab at (c) 300 K and (b) 800 K. Color legend: Fe, orange; Ni, green; C, grey; O, red; H, white.

6.4. Next Steps

6.4.1. Corrosion Experiments

Following the setup of the tube furnaces for these tests, exposure experiments will be completed at 550^{o}C using both research grade and industrial grade CO_2. Both tests will run for a duration of 2000 hours. At each 500 hour interval, samples of each alloy will be pulled from the furnace and characterized for corrosion associated weight gain and corrosion product chemistry (SEM/EDS and XRD)

6.4.2. Thermochemical Modelling

A series of calculations for the equilibrium alloy surface phase/s will be completed for 550^{o}C using FactSage. These will cover the range of alloy chemistry and gas chemistry included in the corrosion experiment test plan. The results from these will be validated against the corrosion product chemistry of experimental samples. Later, these calculations will be extended to investigate the influence of temperature on the equilibrium alloy surface phase/s.

6.4.3. Molecular Dynamics Modelling and Simulation

Further analysis of AIMD simulations of pure CO_2 interacting with (2×2) Fe(100) and Ni(100) slabs is underway. The diffusion of C/O adatoms on both Fe and Ni surfaces will be investigated

and forthcoming simulations will also focus on the CO_2 with impurities. Calculations will also be extended to surfaces with different indices as this information becomes available from experimental characterization.

Electron Backscatter Diffraction (EBSD) of pure Ni and Fe sample surfaces is underway to determine the major crystallographic orientations and other surface properties. The first of two 500 hour exposure tests with high purity Fe and Ni samples in atmospheric pressure CO_2 at both 700K (427^oC) will be started in June. The second 500 hour test at 850K (577^oC) will immediately follow. Samples from both tests will be characterized for surface phase chemistry using SEM/EDS along with Raman spectroscopy.

PAGE INTENTIONALLY LEFT BLANK

7. REFERENCES

1. Dostal, V., Driscoll, M. J., Hejzlar, P., *A Supercritical Carbon Dioxide Cycle for Next Generation Nuclear Reactors* (No. MIT-ANP-TR-100). Cambridge, MA: Massachusetts Institute of Technology, 2004.
2. Gibbs, J. P., Hejzlar, P., Driscoll, M. J., *Applicability of Supercritical CO_2 Power Conversion Systems to GEN IV Reactors* (No. MIT-GFR-TR-037). Cambridge, MA: Center for Advanced Nuclear Energy Systems – MIT Department of Nuclear Science and Engineering, 2006.
3. Choi, Y., Nesic, S., Corrosion Behavior of Carbon Steel in Supercritical CO_2-Water Environments, NACE Corrosion Conference, 2009.
4. Ferguson, J. M., Garrett, J., Lloyd, B., A Multivariate Investigation of the Kinetics of Oxidation of Mild Steels in High Temperature CO_2, British Nuclear Energy Society (BNES) Conference on Corrosion of Steels in CO_2, London, 1974.
5. Gibbs, G. B., A Model for Mild Steel Oxidation in CO_2, Oxidation of Metals, Vol. 7, No. 3, 1973, pp. 173-184.
6. Taylor, M. F., The Application of Thermodynamics to the Oxidation Behavior of Mild Steels in CO_2, Oxidation of Metals, Vol. 16, Nos. 1 / 2, 1981, pp. 133-146.
7. Brierley, R. A., Holmes, D. R., Studies of the Oxidation of 9 and 12Cr steels in high temperature, high pressure CO_2, British Nuclear Energy Society (BNES) Conference on Corrosion of Steels in CO_2, London, 1974.
8. Dewanckel, B., Leclercq, D., Dixmier, J., Holmes, D. R., Corrosion of Unalloyed or Low-Alloyed Steels in Pressurized CO_2, British Nuclear Energy Society (BNES) Conference on Corrosion of Steels in CO_2, London, 1974.
9. German, P. A., Litlejohn, A. C., Oxidation Kinetics of Carbon Steels in Pressurized CO_2-Based Atmospheres at Elevated Temperatures, , British Nuclear Energy Society (BNES) Conference on Corrosion of Steels in CO_2, London, 1974.
10. Propp, W. A., Corrosion in Supercritical Fluids, Idaho National Engineering Laboratory, INEL-96/0180, 1996.
11. American Society for Testing and Materials (ASTM). (2011). "Standard Practice for Preparing, Cleaning, and Evaluating Corrosion Test Specimens." *G1-03*, Philadelphia.
12. Degen, T., Sadki, M., Bron, E., König, U., Nénert, G.; The HighScore Suite; Powder Diffraction / Volume 29 / Supplement S2 / December 2014, pp S13-S18.

13. Dennies, Daniel P, *How to Organize and Run a Failure Investigation*. ASM International, 2005. Print.
14. Pint, B. A., The effect of O_2 and H_2O on Oxidation in CO_2 at 700^o – 800^oC, 5^{th} International Symposium – Supercritical CO_2 Power Cycles, San Antonio, Texas, March 2016.
15. Holcomb, G.R., Dogan, O.N., Materials Performance in Supercritical CO_2 in Comparison with Atmospheric Pressure CO_2 and Supercritical Steam, 5^{th} International Symposium – Supercritical CO_2 Power Cycles, San Antonio, Texas, March 2016.
16. Mahaffey, J., Anderson, M., Sridharan, K., Effect of Oxygen Impurity on Corrosion in Supercritical CO_2 Environments, 5^{th} International Symposium – Supercritical CO_2 Power Cycles, San Antonio, Texas, March 2016.
17. Pint, B. A., The Effect of Temperature and Pressure on Supercritical CO2 Compatibility of Conventional Structural Alloys, 5^{th} International Symposium – Supercritical CO_2 Power Cycles, San Antonio, Texas, March 2016.
18. Kresse, G., Furthmüller, J., *Phys. Rev.* B, 1996, 54, 11169.
19. J. P. Perdew, J. A. Chevary, S. H. Vosko, K. A. Jackson, M. R. Pederson, D. J. Singh, C. Fiolhais, *Phys. Rev.* B, 1992, 46, 6671.
20. J. P. Perdew, K. Burke, M. Ernzerhof , *Phys. Rev. Lett.*, 1996, 77, 3865.
21. E. Kim, A. Mohrland, P. F. Weck, T. Pang, K. R. Czerwinski, D. Tománek, *Chem. Phys. Letters*, 2014, 613, 59.
22. S. Dudarev, G. Botton, S. Savrasov, C. Humphreys, A. Sutton, *Phys. Rev. B,1998,* 57, 1505.
23. P. E. Blöchl, *Phys. Rev.* B, 1994, 50, 17953.
24. G. Kresse, D. Joubert, *Phys. Rev.* B, 1999, 59, 1758.
25. E. R. Davidson, *Methods in Computational Molecular Physics*, G. H. F. Diercksen and S. Wilson, Eds., Vol. 113, NATO Advanced Study Institute, Series C, Plenum, New York, 1983, p. 95.
26. Methfessel, M., Paxton, A.T., *Phys. Rev.* B, 1989, 40, 3616.
27. Monkhorst, H.J., Pack, J.D., *Phys. Rev.* B, 1976, 13, 5188.

DISTRIBUTION

External (electronic)

1 Brian Robinson
US DOE Office of Nuclear Energy
19901 Germantown Rd.
Germantown, MD 20874

1 William Corwin
US DOE Office of Nuclear Energy
19901 Germantown Rd.
Germantown, MD 20874

1 Steven Reeves
US DOE Office of Nuclear Energy
19901 Germantown Rd.
Germantown, MD 20874

1 Bruce Pint
Oak Ridge National Laboratory
One Bethel Valley Road
P.O. Box 2008, MS-6156
Oak Ridge, TN 37831-6156

1 Mark Anderson
University of Wisconsin – Madison
Dept. Engineering Phyiscs
1500 Engineering Dr
Madison WI 53706

1 Kumar Sridharan
University of Wisconsin-Madison
Dept. Engineering Phyiscs
1500 Engineering Dr
Madison WI 53706

Internal (electronic)

1	MS0736	Evaristo Bonano	6220
1	MS1136	Gary Rochau	6221
1	MS1136	James Pasch	6221
1	MS1136	Darryn Fleming	6221
1	MS0747	Philippe Weck	6225
1	MS9161	Christian Mailhiot	8340
1	MS9161	Farid El Gabaly Marquez	8342
1	MS9161	Joshua Sugar	8342
1	MS9403	Matthew Walker	8344
1	MS9403	Alan Kruizenga	8344
1	MS9403	Elizabeth Withey	8344
1	MS9403	Marie Kane	8344
1	MS0899	Technical Library	9536


Sandia National Laboratories